Structural and electronic characterization of nano-sized inorganic materials by X-ray Absorption Spectroscopies

UNIVERSITÀ DEGLI STUDI DI TORINO

E. Borfecchia, G. Agostini, S. Bordiga, E. Groppo, C. Garino, R, Gobetto, A. Agostino, L. Mino, M. Truccato, D. Gianolio, A. Piovano, G. Martinez-Criado, L. Salassa, C. Lamberti,

"Structural and electronic characterization of nano-sized inorganic materials by X-ray Absorption Spectroscopies"

in *Inorganic Micro- and Nanomaterials. Synthesis and Characterization* (A. Dibenedetto M. Aresta Ed.), De Gruyter, Berlin, 2013, p. 93-136.
ISBN: 3110306662; ISBN-13: 9783110306668.

Structural and electronic characterization of nano-sized inorganic materials by X-ray Absorption Spectroscopies

E. Borfecchia[a], G. Agostini[a], S. Bordiga[a], E. Groppo, C. Garino[a], R, Gobetto,[a] A. Agostino[a], L. Mino[a], M. Truccato[b], D. Gianolio[c], A. Piovano,[d] G. Martinez-Criado[e], L. Salassa,[f] C. Lamberti[a,*]

[a]*Department of Chemistry, NIS Centre of Excellence and INSTM Reference Center, Via Giuria 7, University of Turin,10125 Torino, Italy. E-mail carlo.lamberti@unito.it*
[a]*Department of Physics, and NIS Centre of Excellence, Via Giuria 1, University of Turin,10125 Torino, Italy.*
[c]*Diamond Light Source Ltd, Harwell Science and Innovation Campus, OX11 0DE, Didcot, United Kingdom*
[d]*Institut Laue-Langevin (ILL), BP 156 X, F-38042, Grenoble Cedex, France*
[e]*European Synchrotron Radiation Facility (ESRF), 6 Rue Jules Horowitz, 38043 Grenoble, France*
[f]*CIC biomaGUNE, Paseo Miramo´n 182, 20009 Donostia – San Sebastian, Spain.*

1. Introduction

Starting from the late seventies, the progressively increased availability of synchrotron light sources allowed the execution of experiments requiring a high X-ray flux in a continuous interval [1-4] Among them, X-ray absorption spectroscopy (XAS, also known as X-ray absorption fine-structure, XAFS) [5-13] in both near (XANES) and post (EXAFS) edge regions, has became in the last decades a powerful characterization technique in all fields of inorganic chemistry such as catalysis [13-17], organometallic and coordination complexes [18], metal nanoparticles [19,20], electrochemical processes [21,22], coordination polymers or metallorganic frameworks [23], bio-ionorganic molecules including metalloproteins [24-27], chemistry of Actinide and transuranic elements [28], solid state chemistry [12,29-31], etc… .

In this chapter, we will provide a brief introduction to the basic theory of XAS spectroscopy (Section 2), followed by selected examples having some didactic perspective (Sections 3-7). For space limitation, only a fraction of the subjects mentioned above will be discussed, in particular, the chapter will deal with: the reactivity of the $CuCl_2/Al_2O_3$-based catalysts for ethylene oxychlorination (Section 3); the structure, the electronic configuration and the reactivity of Cp_2Cr molecules encapsulated in porous solids (section 4); the structural determination of organometallic complexes in solution (Section 5); the structural determination of the UiO-66 and UiO-667 class of

metallorganic frameworks (Section 6); and the determination of the local structure of on $Al_{xw}Ga_{yw}In_{1-xw-yw}As/Al_{xb}Ga_{yb}In_{1-xb-yb}As$ strained heterostructure grown on InP by metallorganic vapour phase epitaxy (Section 7) as an example of space resolved EXAFS applied to a topic pertinent to solid state chemistry.

2. XAS spectroscopy: basic background

The aim of this section is to provide the reader with a concise review of the basic physical principles on which the interpretation EXAFS and XANES data is based. For a more detailed description of the theoretical background and experimental aspects of XAS we refer to the extensive specialized literature (e.g. [5-13]).

2.1. Theoretical background of XAS spectroscopy.

XAS measures the variations of the X-ray absorption coefficient μ as a function of the incident X-ray energy E. According to the Fermi Golden Rule,[32,33] the XAS signal is proportional to the electron transition probability from the core-state |i> of energy E_i to the unoccupied state |f> of energy E_f, as expressed by Eq.(1), where the product **e·r** indicates the electronic transition dipole operator [7], where $\rho_i(occ)$ and $\rho_f(unocc)$ are the densities of initial occupied and final unoccupied states, respectively, and where $\delta(E_f-E_i-E)$ is a Dirac delta function [12].

$$\mu(E) \propto |< i|\mathbf{e}\cdot\mathbf{r}|f >|^2 \, \delta(E_f - E_i - E)\rho_i(occ)\rho_f(unocc) \qquad (1)$$

The behavior of the $\mu(E)$ function is represented in Figure 1b. A general decrease of the absorption with increasing incident energy can be noticed, following approximately the law [13]:

$$\mu(E)/\rho \approx Z^4/AE^3, \qquad (2)$$

where ρ is the sample density, Z the atomic number and A the atomic mass. This equation holds for a sample containing a unique chemical species like a metal foil, but can be easily generalized for any sample of known composition. In Figure 1b also evident is the presence of the characteristic saw-tooth like edges, whose energy position is a distinctive features of each kind of absorbing atom. These absorption edges correspond to transitions where a core-orbital electron is excited to (i) the free continuum (i.e. when the incident energy is above the ionization energy of the absorber atom) or (ii) unoccupied bond states lying just below the ionization energy. The nomenclature adopted for the edges recalls the atomic orbitals from which the electron is extracted, as shown in Figure 1a: K-edges are related to transitions from orbitals with the principal quantum number n = 1 ($1s_{1/2}$), L-edges refers to electron from the n = 2 orbitals (L_I to $2s_{1/2}$, L_{II} to $2p_{1/2}$, and L_{III} to $2p_{3/2}$orbital), and so on for M, N, … edges.

When the energy of the X-ray photon exceeds the ionization limit (case (i) mentioned above), the excited electron (generally named "photoelectron") has a kinetic energy E_K given by $E_K = h\upsilon - E_B$, where E_B indicates the electron binding energy, that is typical of the absorption edge (K, L_I, L_{II} or L_{III}) of the selected atomic species [13,34]. Once ejected, the photoelectron propagates thorough the sample as a spherical wave diffusing from the absorber atom, with a wavevector of modulus k defined by Eq. (3):

$$k = \frac{2\pi}{\hbar}\sqrt{2m_e E_K} \qquad (3)$$

A close zoom on the energy region in proximity of an absorption edge shows a well defined fine-structure. In particular, only when the absorber is surrounded by neighboring atoms (molecules or crystals) a structure of oscillatory nature modulates the smooth $\mu(E)$ profile at energies above the edge. Figure 1c provides an example for the Cr K-edge spectra of Cp_2Cr in different environments and after interaction with CO. Such modulation in the absorption coefficient derives from the interference between the outgoing photoelectron wave diffusing from the absorber and the wavefronts back-scattered by the neighboring atoms [35,36]. In a typical XAS experiment, the energy range probed around the edge is conventionally divided into two different regions (Figure 1c):

(i) X-Ray Absorption Near Edge Structure (XANES) region: portions of the XAS spectrum just

below and above the edge energy;

(ii) Extended X-ray Absorption Fine Structure (EXAFS) region: portion at higher energies in respect to the edge (from tens to hundreds of eV), characterized by the oscillatory modulation in the absorption coefficient.

Hereby, we will briefly discuss the main information that can be extracted from the analysis of each of the two regions listed above.

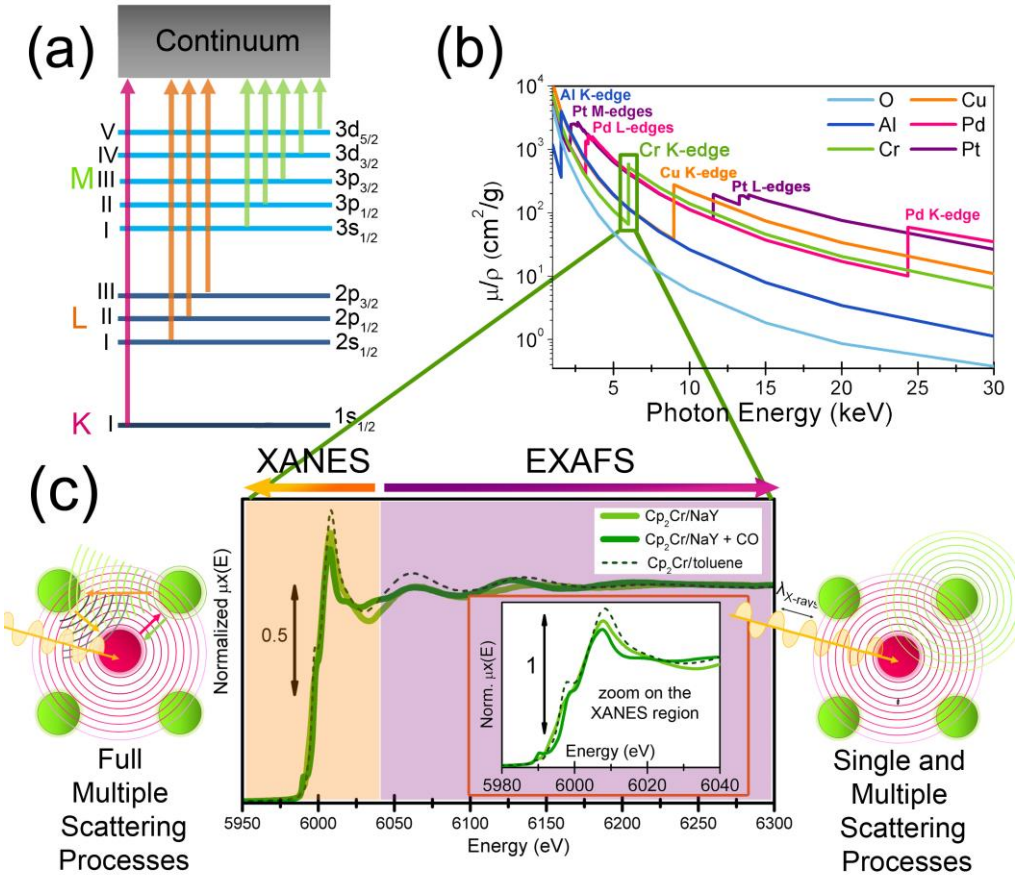

Figure 1. Part (a): X-ray absorption edges nomenclature and representation of their relation with the atomic orbitals from which the electron is extracted. Part (b): General behaviour of the X-ray absorption coefficient μ/ρ, see Eq. (2), as a function of the incident X-ray energy E for O (Z = 8), Al (Z = 13), Cr (Z = 24), Cu (Z = 29), , Pd (Z = 46), and Pt (Z = 78). Data obtained from NIST web site http://physics.nist.gov/PhysRefData/XrayMassCoef/tab3.html. Note the logarithmic scale of the ordinate axis. (c) Cr K-edge XAFS of Cp_2Cr molecule in toluene solvent (dashed line) and hosted inside the cavities of Na-Y zeolite before (light green line) and after (dark green light) interaction with CO [37]. Data collected at BM26A beamline [38] of the ESRF. The conventional division between XANES and EXAFS region and the schematic models of full multiple and single scattering processes, dominating respectively the XANES and EXAFS region, are indicated (color code: absorber atom in magenta; neighbor atoms that back-scatter the photoelectron wave outgoing from the absorber in green). Unpublished figure.

2.2. The XANES region.

The XANES region can be further divided into three main sub-intervals: we can distinguish the pre-edge region, the absorption edge, and the post-edge region, up to 30–50 eV after the edge jump. The investigation of these three portions of the XANES spectrum and the interpretation of the different physical phenomena governing their characteristic features provides plenty of information, both of electronic and structural nature [39].

The pre-edge region can include well defined components, related to electronic transitions from the core level to empty bound states [40], as for example the unoccupied states of the narrow *d*-band lying just above the Fermi energy in transition metals. The features of the pre-edge peaks are directly influenced by the Density of the States (DOS) and the states occupancy, therefore their

investigation is extremely helpful in unraveling the electronic structure of molecules and complexes [7,11]. Moreover, the intensity of pre-edge peaks is governed by the selection rules for dipolar transitions, which can be relaxed depending on the local symmetry around the absorber atom [41]. Pre-edge features related to transitions that are forbidden in the purely dipolar case can however clearly appear in the XANES spectrum, hence providing information about the geometrical coordination environment of the absorber.

The energy position of the absorption edge is sensitive to oxidation state of the absorber due to the charge-shielding effect on the ionization energy: practically a higher oxidation number corresponds to a edge shift towards higher energies [31,42-45]. In addition, the edge location is influenced by the coordination geometry, which ultimately is determined by the molecular orbitals energy position [37,46,47].

The edge and post-edge regions are particularly sensible to the geometrical arrangement of the neighboring atoms in the restricted local cluster around the absorber. This makes XANES a very powerful instrument for direct structural characterization in a wide range of systems, including solids [31,45], solutions [48], surfaces [49] metal nanoparticles [50], and biological samples [51]. The relation between geometrical features and XANES response mainly depends on the multiple scattering processes (Figure 1c) of the excited photoelectron after the ionization threshold, which dominates with respect to the single scattering event due to the lowered photoelectron energy. Moreover, the first 10 eV after the ionization limit are in many cases influenced also by other kinds of physical interactions, directly dependent on the properties of the investigated sample (so-called "shape resonances" in molecules, core excitons in crystals, unoccupied local electronic states in metal and insulators [52]).

2.3. The EXAFS region.

The EXAFS region of the spectrum is located at higher energies and is characterized by the modulation of the absorption coefficient $\mu(E)$. Such feature is caused by the interference between the X-ray waves diffused by the absorber atom and back-scattered by its neighbors. Hence, EXAFS oscillations can be related via Fourier transform to a specific spatial arrangement of the atoms in the local environment of the absorber, bridging the energy space to the real distances *r*-space. This crucial point is at the basis of the EXAFS analysis procedure developed after the milestone works of Sayers, Lytle and Stern [35,36,53].

The higher photoelectron kinetic energy in the EXAFS region implies that the phenomenon is no more dominated by the full multiple scattering regime, that instead dominate in the XANES region [53]; consequently data analysis can be performed using the simpler Fourier transform operation [35];

The EXAFS signal $\chi(E)$ is generally expressed as the oscillatory part of the $\mu(E)$ function, normalized to the edge-jump, i.e. $\chi(E) = [\mu(E) - \mu_0(E)]/\Delta\mu_0(E)$, where $\mu_0(E)$ is the atomic-like background absorption and $\Delta\mu_0(E)$ the normalization factor. Above the absorption edge, the energy *E* can be substituted with the photoelectron wave-vector *k* using Eq. (3), therefore obtaining the EXAFS function $\chi(k)$. The relation between the modulation of the $\chi(k)$ signal and the structural parameters is provided by the EXAFS formula that, in the single scattering approximation, is reported in Eq. (4).

$$\chi(k) = S_0^2 \sum_i N_i F_i(k) e^{-2\sigma_i^2 k^2} e^{-\frac{2r_i}{\lambda(k)}} \frac{\sin\left[2kr_i + 2\delta_l(k) + \theta_i(k)\right]}{kr_i^2} \qquad (4)$$

S_0^2 is the overall amplitude reduction factor; the index i runs over all the different shells of neighboring atoms around the absorber, $F_i(k)$ is the back-scattering amplitude as a function of *k* for each shell, in N_i is the coordination number (number of equivalent scatterers), σ_i is the Debye-Waller factor accounting for thermal and static disorder. The parameter r_i indicates the interatomic distance of the *i*-th shell from the central absorber. The phase shift of the photoelectron is distinguished in two contributions, related to the absorber ($2\delta_l$) and to the scatterer (θ_i).

In Eq. (4) the electron back-scattering amplitude $F_i(k)$ is measured in Å [54,55]. Indeed $F_i(k)$ defines the weight that the i-th neighbor has in the overall EXAFS signal. As the electron scattering is mainly performed by the electron clouds of the neighbor atoms, it is evident that $F_i(k)$ will be larger for larger Z neighbors. Consequently, as was the case for X-ray scattering, EXAFS will be less efficient in the detection of low Z neighbors and the discrimination among neighbors having similar Z will be critical. When the difference in Z is sufficiently large, then both back-scattering amplitude $F_i(k)$ and phase shift functions are markedly different to allow an easy discrimination between the different neighbors.

The presence of the phases terms $2\delta(k) + \theta(k)$ inside the sinus function is the reason why the FT of the raw $k^n\chi(k)$ functions always reports a peak in R-space at 0.2-0.4 Å shorter distance with respect to the true distance. Only a phase corrected FT results in a distances distributions in R-space centered around the correct value, vide infra the discussion in Section 3.2.1 and Figure 2b,c,d.

The term $\lambda(k)$ is the energy-dependent photoelectron mean free path, typically few Å [56], determining the local nature of the technique that can investigate only up to ≈ 5–8 Å around the photo-excited atom. This apparent limitation of EXAFS is conversely a big advantage in the investigation of disordered materials like glasses or liquids as the long range order is not required [57].

Coming to the Debye-Waller term $\exp(-2\sigma_i^2k^2)$, it has the same physical origin of the term $\exp(-q^2u_n^2/6)$ used to refine diffraction experiments [58,59]. Actually the thermal parameters σ_i^2, measured in an EXAFS experiment, and $u^2_{n,a}$, $u^2_{n,b}$, $u^2_{n,c}$, measured in a diffraction experiment, represents two different aspects of the atomic vibrations in crystals. The anisotropic mean squared displacements $u^2_{n,a}$, $u^2_{n,b}$, $u^2_{n,c}$, or the isotropic mean squared displacement u^2_n measure how the *n*-th atom vibrates inside the unit cell along **a**, **b** and **c** directions (u^2_n being an average of $u^2_{n,a}$, $u^2_{n,b}$, $u^2_{n,c}$). The σ_i^2 parameter measures how the couple of atoms absorber–*i*-th shell neighbor vibrates along the direction that connect these two atoms. This means that in case of strongly correlated vibrations, the scatterer and the absorber can vibrate in phase, resulting in a low σ_i^2 parameter and in a larger u^2_n parameter.

The standard EXAFS formula, Eq. (4), provides a convenient parameterization for fitting the local atomic structure around the absorbing atom to the experimental EXAFS data [60] The dependence of the oscillatory structure of the EXAFS signal on interatomic distance and energy is clearly reflected in the $\sin(2kr_i)$ term. The strength of the interfering waves depends on the type and number of neighboring atoms through the backscattering amplitude $F_i(k)$ and the coordination number N_i, and hence is primarily responsible of the magnitude of the EXAFS signal. Once the phase and amplitude functions have been independently measured on model compounds or *ab initio* computed, the structural parameters N_i, r_i, and σ^2_i, can be determined in a least square approach where the difference between the experimental and the modeled $k^n\chi(k_j)$ function is minimized along all the sampled experimental points k_j. The minimization routine can be done either in *k*-space, directly on the measured $k^n\chi(k_j)$ function, or in *r*-space, working on the Fourier-transformed functions. So, for each coordination shell, the coordination number, the atomic distance and the thermal factor can be extracted from an accurate EXAFS study. Extending the Nyquist-Shannon theorem [61,62] (also known as sampling theorem) to the EXAFS case, the maximum number of optimized parameters cannot exceed the number of truly independent points (n_{ind}), where n_{ind} is defined by the product of the sampled interval in *k*-space (Δk) and the interval in *R*-space(ΔR) containing the optimized shells:

$$n_{ind} = 2\Delta k\Delta R/\pi. \qquad (5)$$

A careful monitoring of the fitting results is fundamental to avoid local or non physical minima of the minimization process. Analogously, correlation parameters between each couple of optimized parameters should ideally be lower than 0.8 in absolute value and should never exceed 0.9. Eq. (5) underlines the importance of acquiring the EXAFS spectrum over the largest possible *k*-interval. Experimental data collected up to a high maximum *k*-value k_{max} allows to: (i) increase

n_{ind}, as Δk increases; (ii) reduce the correlation between N_i and σ_i parameters; (iii) increase the ability to discriminate between two close distances. The distance resolution (Δr) of an EXAFS spectrum is indeed defined from k_{max} according to the relation:

$$\Delta r = \pi/(2\ k_{max})\ . \qquad (6)$$

Two equally intense signals generated by the same scatterer located at r_1 and r_2 can indeed be singled out only in case the two oscillating functions $\sin(2k\ r_1)$ and $\sin(2k\ r_2)$ are able to generate at least a beat in the sampled k-range, and this occurs for $2k(r_1 - r_2) = \pi$. Consequently, in order to reach a distance resolution of $\Delta r = 0.1$ Å the EXAFS spectrum has to be collected up to about 16 $Å^{-1}$. The Δr parameter reported in Eq. (6) is the EXAFS-equivalent of the d-spacing parameter in diffraction experiments, obtained from the Bragg equation as $d_{min} = \lambda/[2\ \sin(\theta_{max})]$, and that define the accuracy in the reconstruction of the electron density.

2.4. Advantages and drawback of the technique.

In a very concise way, we can summarize the main advantage of XAFS technique as follows:

(i) The atomic selectivity, allowing to get information from the selected atomic species only.

(ii) The accessibility to very diluted species;

(iii) The relative high penetration depth of hard X-rays makes possible experiments on samples in contact with liquid or gases. This aspect is very important in catalysis, as in situ or operando experiments can be done.

(iv) The local nature of the X-ray absorption phenomenon, limited by the photoelectron mean free path λ see Eq. (4), does not require long range order, making liquids, gases and amorphous systems accessible to the investigation.

Using the same concise style, the main drawbacks of the technique can be summarized as follows.

(i) For most of case of real interest, laboratory X-ray sources, using the Bremsstrahlung radiation emitted by rotating anodes has a non sufficient flux and synchrotron radiation sources are needed.

(ii) Homogeneity of the sample is the main request of the technique. If the dominant fraction (larger than 90%) of the selected atomic species has the same local environment, then the coordination numbers and the bond-lengths extracted from the EXAFS data analysis are reliable. In case of presence of several phases, then it is much more critical, although not impossible, to extract quantitative information from EXAFS. In such cases the use of complementary information from independent techniques represents a fundamental approach to avoid misleading results. Examples on how to handle EXAFS data analyses when more phases are present are described in Sections 3.2.3, and 4.3. Alternatively, a way to overcame space heterogeneity of the sample, using μm-focused X-ray beams is reported in Section 7.

(iii) Owing to the large absorption of high Z-elements, see Figure 1b, the EXAFS performed on relatively light elements embedded in matrices containing high Z elements is particularly critical.

3. $CuCl_2/Al_2O_3$–based catalysts for ethylene oxychlorination.

3.1. Industrial relevance of the $CuCl_2/Al_2O_3$ system.

Nowadays, almost all the world production of PVC chloride (PVC) is based by the polymerization of vinyl chloride, which is produced by cracking of 1,2-dichloroethane (EDC), according to the following reaction:

$$C_2H_4Cl_2 \rightarrow C_2H_3Cl + HCl \qquad (7)$$

$C_2H_4Cl_2$ is in turn obtained by two parallel processes, direct chlorination (8) and oxychlorination (9):

$$C_2H_4 + Cl_2 \rightarrow C_2H_4Cl_2 \qquad (8)$$

$$C_2H_4 + 2HCl + ½\ O_2 \rightarrow C_2H_4Cl_2 + H_2O \qquad (9)$$

The latter reaction, recycling HCl produced by the cracking of EDC, is particularly important in industrial applications because it was specifically developed to reduce the consumption of Cl_2 and the exit of useless product (HCl) outside the cycle, in agreement with the modern requests of chemical industry [63] that need more environmental friendly reactions. Oxychlorination of ethylene offers a significant economic benefit in two ways: firstly, it uses cheap and abundant feedstock and, secondly, it incorporates the recycling of waste HCl produced in the cracking EDC (7).

Oxychlorination reaction (9) is performed at 490-530 K and 5-6 atm using both air and oxygen in fluid or fixed bed reactors. Commercial catalysts are produced by impregnation of γ-alumina with $CuCl_2$ (4-8 wt% Cu). Other metal-chlorides (mainly alkaline or alkaline earth chlorides) in a variable concentration are also added in order to improve the catalytic performances, making the catalyst more suitable for use in industrial reactors. In particular, KCl is always present in the catalysts used in fixed bed technologies, sometimes together with other alkali-metal chlorides, such as CsCl, NaCl or LiCl. Rare-earth-metal chlorides such as $LaCl_3$, added to $CuCl_2$ and KCl, are also claimed in the patent literature. $MgCl_2$ is the base additive in the catalysts used in fluid bed processes, where alkali-metal (such as LiCl) or rare-earth-metal chlorides (such as $LaCl_3$) can also be added.

3.2. Preliminary in situ XAFS experiments.

In the 2000-2003 period Leofanti et al achieved a significant improvement of the knowledge of the undoped $CuCl_2/Al_2O_3$ system [64-68]. In those studies several complementary techniques were adopted and, among them, EXAFS and XANES played a key role. Indeed the $CuCl_2$ phase is so dispersed on the γ-Al_2O_3 support that even at a loading level as high as 9 wt. % it is XRD silent [65] This made EXAF the only structural technique available for this system. XANES was widely used to determine the oxidation state of the active phase under the different catalyst conditions. In those studies It has been proved that two different copper species are present on the activated catalyst (dried at 500 K in N_2 flux): a surface copper aluminate, where the copper ions are hosted in the octahedral vacancies of γ-Al_2O_3, and a highly dispersed copper chloride phase. The former phase is the only one present at low Cu loadings (up to 0.95 wt% Cu per 100 m^2 support); the latter precipitates directly from the solution once that the adsorptive capacity of alumina is exhausted [66-68].

3.2.1. The determination of the Cu-aluminate phase: how to avoid possible pitfalls in the EXAFS data analysis. When using Eq. (4) to fit the experimental EXAFS data, care must be done to apply the correct structural model, i.e. to hypothesize the correct atomic species surrounding the absorbing atom that contributes to the scattering process of the photoelectron. Indeed the applied model defines the amplitude $F(k)$ and phase $\theta(k)$ functions used in the fit. A wrong choice of the model will result in misleading results. The case of the Cu-aluminate phase mentioned so far is didactically emblematic to discuss this matter.

The Cu-aluminate phase was evidenced on a sample loaded with only 1.4 Cu wt. % (hereafter Cu1.4) [67]. As the catalyst is prepared following the incipient wetness impregnation of a γ-Al_2O_3 with an aqueous solution of $CuCl_2$ $2H_2O$, two chemically reasonable possibilities are possible to model the first coordination shell around copper: (i) upon drying Cu^{2+} recombine with Cl^- cation forming dispersed $CuCl_2$ phase; or (ii) upon drying Cu^{2+} occupies the cationic vacancies of the defective γ-Al_2O_3 support. Following model (i), Cu-Cl phases and amplitudes are adopted in Eq. (4) and the fit results in the bottom curves reported in Figure 2a. Adopting model (ii), Cu-O phases and amplitudes are adopted and the fit results in the top curves reported in Figure 2a. Model (ii) is preferred for he following reasons: (a) the better quality of the fit obtained with the Cu-O model (defined by the R- and χ^2-facors); (b) the reasonable values of the optimized parameters ($N = 4.8 \pm 0.5$; $r_{Cu-O} = 1.92 \pm 0.02$ Å: $\sigma = 8.9 \times 10^{-2}$ Å); (c) the result of the statistical F-test [69].

When comparison between the two models is made no doubt on the right model is possible; but what's if only model (i) was consider? What's if we were not able to put forward model (ii) form

the beginning? Having only model (i) could we realize that this is a wrong model? In this specific case the answer is yes, and we will report here two different methodological approaches that will allow to discard model (i), independently on the availability of an alternative model. The first approach consists in a simple comparison of the FT transform of the unknown material with those of model compounds, where the structural environment of the adsorbing atom is well established. Figure 2b reports the comparison between sample Cu1.4 and $CuCl_2$ $2H_2O$ model compound. The first coordination shells of Cu^{2+} in hydrated $CuCl_2$ exhibits two oxygens at 1.95 Å and two chlorines at 2.29 Å, responsible for the two peaks at 1.48 and 1.93 Å in the phase uncorrected FT of the EXAFS function reported as green curve. As discussed in Section 2.3, without any phase correction, i.e. performing the FT of the experimental $\chi(k)$ without considering the phase $2\delta(k) + \theta(k)$ terms inside the sinus function in Eq. (4), the peaks of the radial distribution in the R-space always occurs at shorter distances with respect to the real ones. Besides this technical aspect, it is evident that the radial distribution of sample Cu1.4 is not compatible with a Cu-Cl contribution, as it appears at a significantly shorter distance.

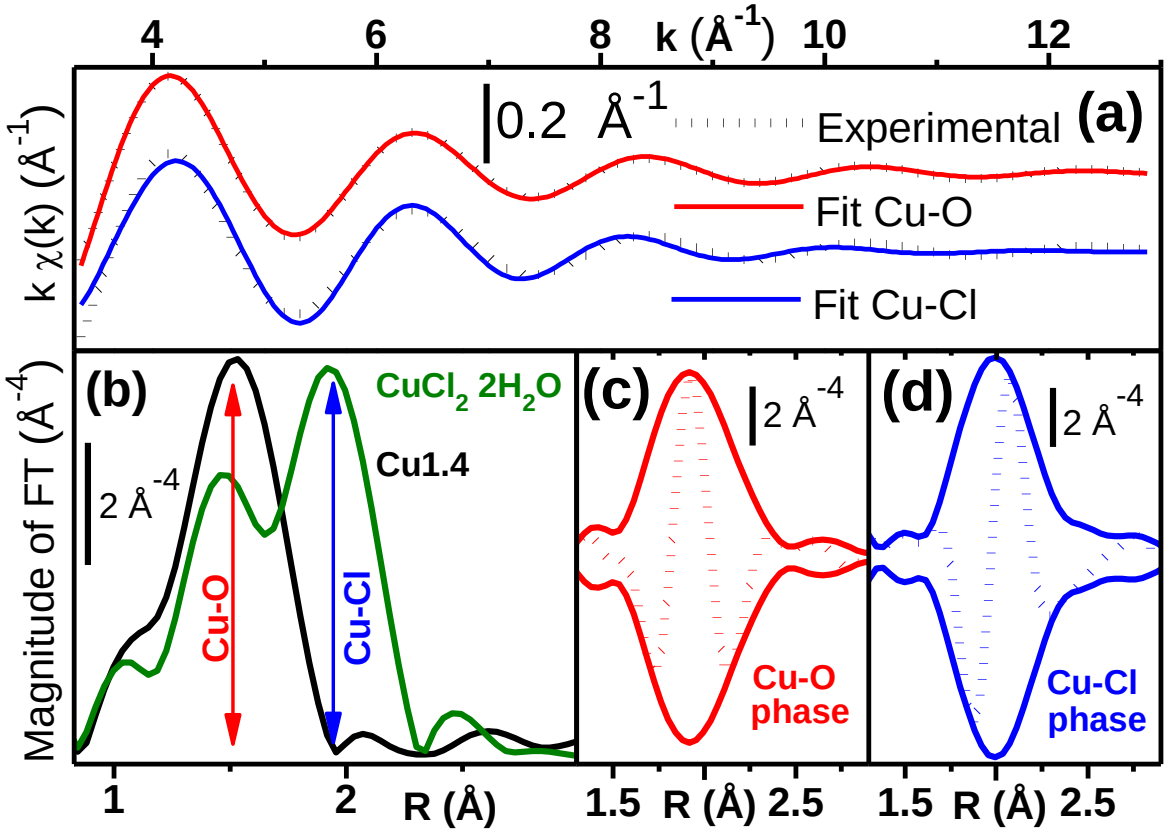

Figure 2. Part (a): First shell filtered of the experimental EXAFS curve $k\chi(k)$, (black dotted lines) and comparison with best fit obtained using Cu–O (red curve) and Cu–Cl (blue curve) models. Part (b): k^3-weighted, phase-uncorrected, FT for the Cu1.4 sample and $CuCl_2$ $2H_2O$ model compound, black and green curves, respectively. Part (c): modulus (full line) and imaginary part (dotted line) of the k^3-weighted and Cu–O phase-corrected, FT for the Cu1.4 sample. Part (d): as part (c) using the Cu–Cl phase for the correction. Unpublished figure, reporting data published in Ref. [67].

The second approach consists in the application of the Lee and Beni criterion [70]. This criterion affirms that when a given coordination shell of the absorbing atom A (the first in our case) is composed by only one atomic species B, located at the same distance (or with a very small spread in the distances), then the FT of the experimental $\chi(k)$ corrected by the $2\delta(k) + \theta(k)$ phase of the A-B couple will result in a radial distribution function centered at the right distance and having an imaginary part that is symmetric with respect to its modulus. Performing the FT of the $\chi(k)$ of sample Cu1.4 corrected by the Cu-Cl phases we obtain the radial distribution reported in Figure 2d. The fact that the imaginary part of that phase corrected FT is not symmetrical with respect to its modulus automatically discards the model of a first shell of Cu^{2+} in Cu1.4 sample made by Cl atoms. Actually,

it discards the fact that the first shell is made by only (or mainly) Cl atoms, but it can not discard that some Cl atoms contribute (in a minority way to the first shell signal of Cu1.4. sample. The final proofs that in the first coordination of Cu^{2+} in Cu1.4 there are only O atoms, and thus that a Cu aluminate phase has been formed, is given by Figure 2d, showing that using Cu-O phases, the obtained FT has an imaginary part that is perfectly symmetrical with respect to its modulus.

3.2.2. Catalyst reactivity with the separate reactants: in situ XAFS experiments

Successively it has been shown that the active phase in ethylene oxychlorination reaction (9) is the highly dispersed $CuCl_2$. following the three steps redox mechanism reported below [64,65]:

$$2CuCl_2 + C_2H_4 \rightarrow C_2H_4Cl_2 + 2CuCl, \quad (10)$$

$$2CuCl + \tfrac{1}{2} O_2 \rightarrow Cu_2OCl_2 , \quad (11)$$

$$Cu_2OCl_2 + 2HCl \rightarrow 2CuCl_2 + H_2O \quad (12)$$

This redox cycle, has been determined by means of an in situ Cu K-edge XANES and EXAFS study, where the three reagents (C_2H_4, O_2 and HCl) have been separately dosed on the activated $CuCl_2/\gamma$-Al_2O_3 at 500 K in the given order (see Figure 3). In particular, the chlorination of ethylene, Eq. (10), occurs by reduction of $CuCl_2$ to CuCl, as testified by the red-shift of the Cu K-edge, see Figure 3a top curves. The oxidation of CuCl to an oxychloride, Eq. (11), is proved by both the opposite blue-shift of the Cu K-edge and the appearance of a low-R contribution in the |FT| of the EXAFS spectra, due to the insertion of oxygen in the first coordination sphere of Cu, see middle curves in Figure 3a and b, respectively. Finally, the catalytic cycle is closed by the re-chlorination of the oxychloride phase with HCl, Eq. (12), as demonstrated by the disappearance of the above mentioned oxygen contribution in the FT of the EXAFS spectrum, see red curve in the bottom of Figure 3b.

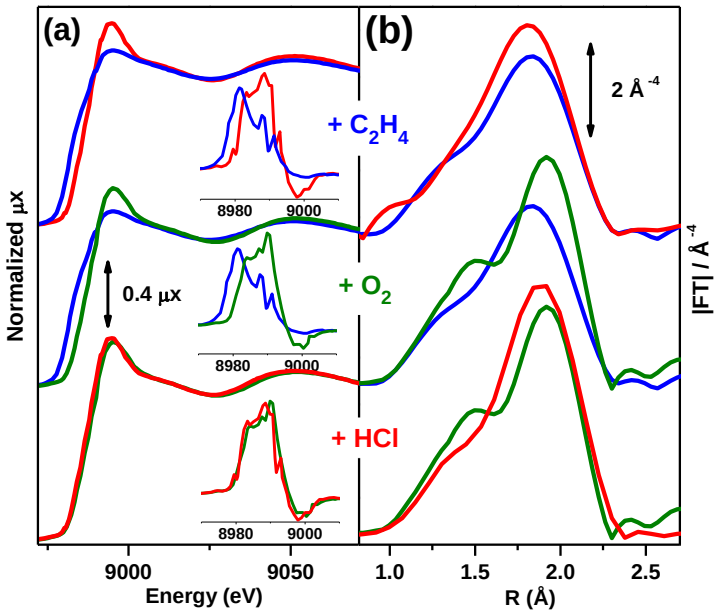

Figure 3. Three steps redox mechanism of the ethylene oxychlorination reaction, Eq. (10)-(12) followed by in situ XANES and EXAFS, parts (a) and (b), respectively. From top to bottom the effect of the separate and successive dosage of the three reagents is reported: activated catalyst before (red line) and after (blue line) ethylene interaction; reduced catalyst before (blue line) and after (green line) interaction with O_2; oxidized catalyst before (green line) and after (red line) interaction with HCl. In all cases the interaction temperature was 500 K. Insets in part (a) report the derivative of the spectra reported in the main part. Unpublished figure reporting data collected at LURE DCI (EXAFS13 beam line) from Refs. [64,65]; reproduced with permission from Ref. [13], copyright American Chemical Society 2013.

The spectra shown in Figure 3a demonstrate that the oxidized and the reduced form of the catalyst are easily recognizable by XANES spectroscopy. In particular, XANES spectrum of the oxidized catalyst is characterized by an intense white line at 8995 eV, while that of the reduced catalyst shows a less intense white line at 8993 eV and exhibits a red shift of the edge of 5 eV. Even more informative are the derivative spectra (see insets), where the oxidized catalyst exhibits a strong maximum at 8988 eV and a negative peak at 8998 eV, while the reduced catalyst shows a maximum at 8981 eV.

More recently Muddada et al. [43,44,71,72] extended the works of Leofanti et al. [64-68] from the bare to the LiCl-, KCl-, CsCl-, $MgCl_2$- and $LaCl_3$-doped $CuCl_2/Al_2O_3$ catalysts. Combining in situ XANES/EXAFS, IR spectroscopy of adsorbed CO, CO chemisorption and catalytic tests performed using a pulse reactor in depletive mode authors succeeded in understanding the role of dopants (LiCl, KCl, CsCl, $MgCl_2$ $LaCl_3$) in determining the nature, relative fraction, reducibility and dispersion of Cu-phases on $CuCl_2/\gamma$-Al_2O_3 catalysts for oxychlorination reaction (vide infra the main parts of Figure 5 for the reduction by ethylene at 500 K. Eq. (10)). As already discussed above from the previous works it was known that in the undoped catalyst two Cu phases coexist: Cu-aluminate and supported $CuCl_2$, being the latter the only active one [66]. In particular, the EXAFS and XANES data demonstrated the following trend in the ability of the dopant cation to compete with Cu^{2+} in the aluminate phase formation has been found: $K^+ \leq Cs^+ \leq Li^+ << Mg^{2+} < La^{3+}$ [44]. In particular, a fraction close to 100% of copper in the active phase is obtained by adding $MgCl_2$ or $LaCl_3$ dopants. Moreover, EXAFS directly, and IR indirectly, proved that the addition of KCl or CsCl (and less efficiently of LiCl) promotes the formation of mixed CuK_xCl_{2+x} or $CuCs_xCl_{2+x}$ phases, so altering the chemical nature of the active phase. XANES spectroscopy indicates that addition of $MgCl_2$ or $LaCl_3$ does not affect the reducibility by ethylene of the active $CuCl_2$ phase and that the reducibilility of the new copper-dopant mixed chloride are in the order $CuCl_2 > CuLi_xCl_{2+x} > CuK_xCl_{2+x} > CuCs_xCl_{2+x}$ [44], (vide infra the main parts of Figure 5).

3.3. Operando experiments and criteria used to face the presence of more than one phase in the sample.

The determination of the rate determining step , among reactions (10)-(12) has been successively achieved by a time resolved XANES operando study [42,73]. The experiment was performed by feeding a cell containing a self-supported thin pellet of the catalyst with a diluted mixture of the three reagents (C_2H_4:HCl:O_2:N_2 = 100:36.1:7.6:180), representative of the fixed-bed process. In the course of the experiment the temperature was increased from 373 to 623 K and then decreased again to 373 K. Time resolved XANES spectra were collected in dispersive geometry and the catalyst activity was simultaneously analyzed with a quadrupole mass spectrometer. The results of the experiment are summarized in Figure 4, part (a) for the heating step and part (b) for the cooling step of the experiment. The top curves in parts (a,b) report the evolution of the XANES spectra, while the bottom curves correspond to their first derivatives Figure 4c summarizes the evolution of the Cu^{2+} fraction (red, orange and magenta curves) estimated from the XANES and compared with the catalyst activity reported in terms of oxygen consumption (scattered blue dots).

The XANES spectra reported in Figure 4a,b indicate a progressive reduction of Cu^{2+} into Cu^+ during the heating step whereas almost no changes are observed in the XANES spectra collected in the cooling step. To evaluate the Cu^{2+} fraction, for each spectrum along the heating or cooling step, two model spectra are needed, one for the fully oxidized catalyst and one for the fully reduced. The catalyst itself, after activation in N_2 flux up to 500 K before and after reduction in C_2H_4 atmosphere at 500 K has been used for this purpose. Three independent methods have been used to quantify the fraction of Cu^{2+} belonging to the active phase on the catalyst in the i-th spectrum, x_i. The first method concerns in determining the energy (E_i) position of the edge, arbitrarily defined as the energy corresponding to normalized $\mu x = 0.5$:

$$x_i = (E_i - E_{Red})/(E_{Ox} - E_{Red}) \qquad (13)$$

where E_{Ox} and E_{Red} are the energy of the edge in the oxidized and reduced reference spectra respectively; and E_i the position of the edge in the i-th spectrum. Cu^{2+} fractions evaluated from this method are reported as red lines in Figure 4c.

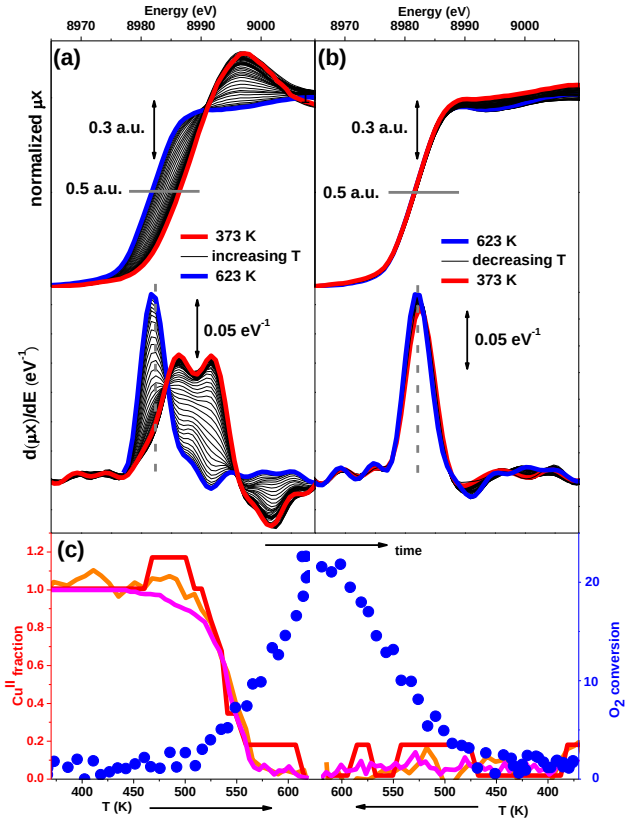

Figure 4. Part (a): XANES spectra (top) and corresponding derivatives (bottom) of $CuCl_2/Al_2O_3$ system in ethylene oxychlorination environment, during the heating step of the experiment (from 373 K, blue curve, to 623 K, red curve, by 12 K min^{-1}). Part (b) as part (a) for the cooling step of the experiment (from 623, red curve, to 373 K, blue curve, by 12 K min^{-1}). XANES spectra have been collected each 30 s, corresponding to a ΔT of 6 K. Part (c) summarizes the results of the operando experiment (both heating and cooling steps, left and right parts, respectively), by correlating the catalyst activity, monitored as O_2 consumption (dotted scattered blue points, right ordinate axis) with the fraction of Cu^{2+} (left ordinate axis) red, orange and magenta lines, evaluated according to methods reported in Eqs. (13), (14) and (15)-(16), respectively. Figure reporting data collected at ESRF ID24 beam line and published in Refs. [42,73]; reproduced with permission from Ref. [13], copyright American Chemical Society 2013.

The second method uses the intensity (I) of the first maximum due to the Cu^+ component in the derivative spectra at 8982 eV:

$$x_i = 1 - I_i/I_{Red,} \qquad (14)$$

Where I_{Red} refers to the spectrum of the reduced reference. Cu^{2+} fractions evaluated from this method are reported as orange lines in Figure 4c. The peak at 8981 eV has been chosen because it is the most intense feature of the derivative XANES spectra of Cu^+ species and it falls in a region where the Cu^{2+} species have a null derivative. This method can not be translated to directly measure the fraction of Cu^{2+} using the most intense Cu^{2+} features at 8985 and 8992 eV, because in this region the derivative of Cu^+ species is still strong.

The last method consists in the simulation of the i-th spectrum as the lineal combination of the two reference spectra according to Eq. (15) [31,45,68,73]:

$$Xanes^{Theo}{}_i(E_j, x_i) = x_1\, Xanes^{Ox}(E_j) + (1\text{-}x_i)\, Xanes^{Red}(E_j) \qquad (15)$$

The fraction of oxidized copper species, x_i, is optimized by a least squares method,

$$\mathbf{F}(x_i) = \sum_{j=1}^{N}\left[Xanes_i^{Exp}(E_j) - Xanes^{Theo}(E_j, x_i)\right]^2 \qquad (16)$$

where E_j (j = 1, 2, … N) are the energies where the experimental spectra have been sampled. Cu^{2+} fractions evaluated from this method are reported as magenta lines in Figure 4c. Although this last method is more time-demanding that the previous ones, it is also more accurate, as it accounts for all the points of the spectrum.

Comparing, in Figure 4c (left axis), the fraction of Cu^{2+} species (x_i) evaluated according to methods (13), (14) and (15)-(16) for the series of spectra reported in Figure 4a,b we can conclude that in all cases the agreement among the three methods is rather good, as they provide values in relative agreement within ± 5%. It is interesting to note that the x_i fraction evaluated according to method (13) has a step-like trend, because of the discreteness of the energy scale measurable with a position-sensitive detector.

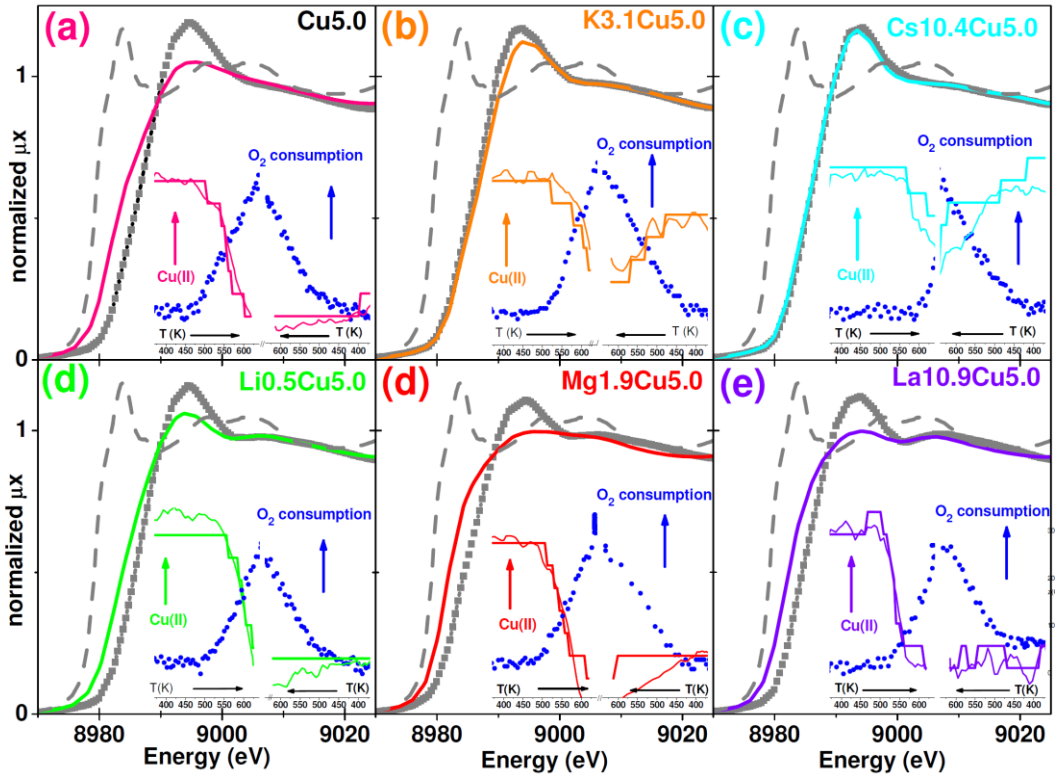

Figure 5. Main parts: XANES static spectra (LURE DCI, EXAFS13 beam line) of doped samples before (grey scattered curves) and after (colored solid lines) reduction by ethylene at 500K compared with a spectrum of pure Cu^{I} chloride (dashed grey line; same curve in all frames). The insets show the results of operando experiments (ESRF ID24 beam line) reporting the evolution of the Cu^{II} fraction along the heating and cooling runs estimated from the edge shift (Eq. (13) bold colored line) and from the intensity of the maximum of the first derivative (Eq. (14) full colored line) together with the catalyst activity (scattered blue dots). Figure reporting data published in Refs. [43,44,72]; reproduced with permission from Ref. [13], copyright American Chemical Society 2013.

From the whole set of data summarized in Figure 4c the following can be commented. At the starting point (373 K) only Cu^{2+} is present and the catalyst is inactive. Both O_2 conversion and Cu^{2+} reduction start in the same temperature range (470-490 K) and progressively increase upon increasing the temperature. Cu^{2+} reduction is completed at 600 K, see Figure 4c. During the cooling step, O_2 conversion progressively declines becoming negligible in the 490-470 K range, while the oxidation state of Cu does not change anymore. These results provide evidence that at the typical oxychlorination temperature, Cu^{+} is the dominant phase and the rate determining step is the oxidation of CuCl, according to Eq. (11). In order to understand the low efficiency of the oxidation process, the catalyst at the end of the cooling step has been subjected to two different oxidizing treatments at increasing temperatures (373-623 K): the former with diluted O_2, the latter with a diluted O_2-HCl mixture. The first treatment causes the complete Cu oxidation already at 373 K, while the second leaves the Cu^{+} unchanged up to 550 K, and, even at 623 K, Cu^{+} is still present.

Authors concluded that HCl acts as poison for Cu^+ oxidation and is responsible for the prevailing reduced state of copper during reaction [42].

The key role of potassium chloride dopant, present in the industrial catalysts used in fixed bed technologies, has been highlighted in a similar experiment [42]. It has been shown that the $KCl/CuCl_2/\gamma\text{-}Al_2O_3$ catalyst behaves differently from the base one, working in a prevailing oxidized state (Figure 5b). Combining operando XANES experiments with catalytic tests of ethylene conversion in pulse reactors and with IR experiments of adsorbed CO, it was concluded that the active phase of the $KCl/CuCl_2/\gamma\text{-}Al_2O_3$ is a mixed chloride (K_xCuCl_{2+x}) phase [42], which reduces the ability of the active surface to adsorb ethylene and/or transfer two Cl atoms to each ethylene molecule. Although not detectable by XRD owing to too small crystal size [66], the formation of the mixed-chloride double compound, was suggested by IR spectroscopy of adsorbed CO [42].

More recently, Muddada et al. [43] extended the works of Lamberti et al. [42,73] to the LiCl-, CsCl-, $MgCl_2$-, $CeCl_4$- and $LaCl_3$-doped $CuCl_2/Al_2O_3$ catalyst. Some of these results are summarized in Figure 5. Authors coupled the catalyst activity (monitored with a pulse reactor working in both non-depletive and depletive modes) with time resolved XANES spectroscopy performed under operando conditions (as done for the undoped catalyst, Figure 3 and Figure 4); they succeeded in understanding, at the atomic level, the role played by additives in the chemistry of the industrial catalyst used in the ethylene oxychlorination. Both KCl (Figure 5b), and CsCl (Figure 5c), form in reaction conditions a mixed phase with $CuCl_2$, which strongly modify the catalyst behaviour [43]. In particular, these additives were able to reverse the rate determining step, from the CuCl oxidation (typical of the undoped catalyst) to the $CuCl_2$ reduction i.e. from Eq. (11) to Eq. (10). The change in the rate determining step is a consequence of the decrease of the rate of the latter reaction, thus of the overall activity of the system. For all remaining additives (Figure 5d-f)the rate determining step remains the CuCl oxidation, as for the undoped catalyst [43], because the additive chlorides does not mix with $CuCl_2$, that remains the active phase.

4. Structural and electronic configuration of Cp_2Cr molecules encapsulated in PS and Na-Y zeolite and their reactivity towards CO

In the last decades many efforts were devoted to find new methods for metal incorporation and catalyst immobilization inside nanoporous scaffolds [74]. Inside of this wide field of research, the inclusion of organometallic complexes inside host frameworks gives the possibility of disparate applications such as electronic devices, optical materials or heterogeneous catalysis [75,76], assuming even more interest.

Metallocenes are organometallic substrates used to investigate potential reactivity enhancement; among them, Chromocene(Cp_2Cr) is a challenging candidate both for applicative reasons, being precursor of the well known Union Carbide olefin catalyst [77], and for theoretical causes since there is still a challenging problem in modeling open shell kind of molecules.

As well as theory has not been able to solve alone all the open questions on this topic, even the experimental approaches adopted so far to investigate properties and reactivity of these system (such as matrix isolation technique [78] and dissolution in a solvent [79,80]), suffered of some disadvantages and the results were not such in agreement with ab initio calculations. The problems consisted in the air sensitivity of the molecules of Cp_2Cr (that enforce to work in controlled atmosphere) and their tendency to form cluster, so that most of the techniques give information about the clusters and not about the isolated molecules or about the active species useful for the catalysis.

4.1. Structure of Cp_2Cr encapsulated in PS and Na-Y zeolite matrices

Estephane et al. [37,81-83] developed new strategies to obtain spectroscopic information on isolated molecules and on their reactivity, in particular towards CO. Two matrices were adopted as "scaffolds" to encapsulate and isolate molecules in their cavities:

- A non polar nanoporous Polystyrene (PS) matrix (average dimensions of pores 100 Å, high surface area ≈ 1000 m^2g^{-1}) that can act as a "solid solvent" molecularly dispersing the Chromocene inside his nanopores (Figure 6a).
- A polar Na-Y Zeolite (Figure 6b), that is expected to enhance the reactivity of the hosted molecules by means of the internal electrostatic fields. In fact zeolitic voids would function as "nanoscale reaction chambers", where the reactivity of guest organometallic complexes can provide molecular insights into the elementary steps of heterogeneous catalysis.

A systematic XAFS and IR study allowed the authors to obtain a complete structural, electronic and vibrational insight the isolated molecule and of its interaction products with CO (sent in gas phase so easily diffusing in the porous matrices) in the two different environments [37,81-83].

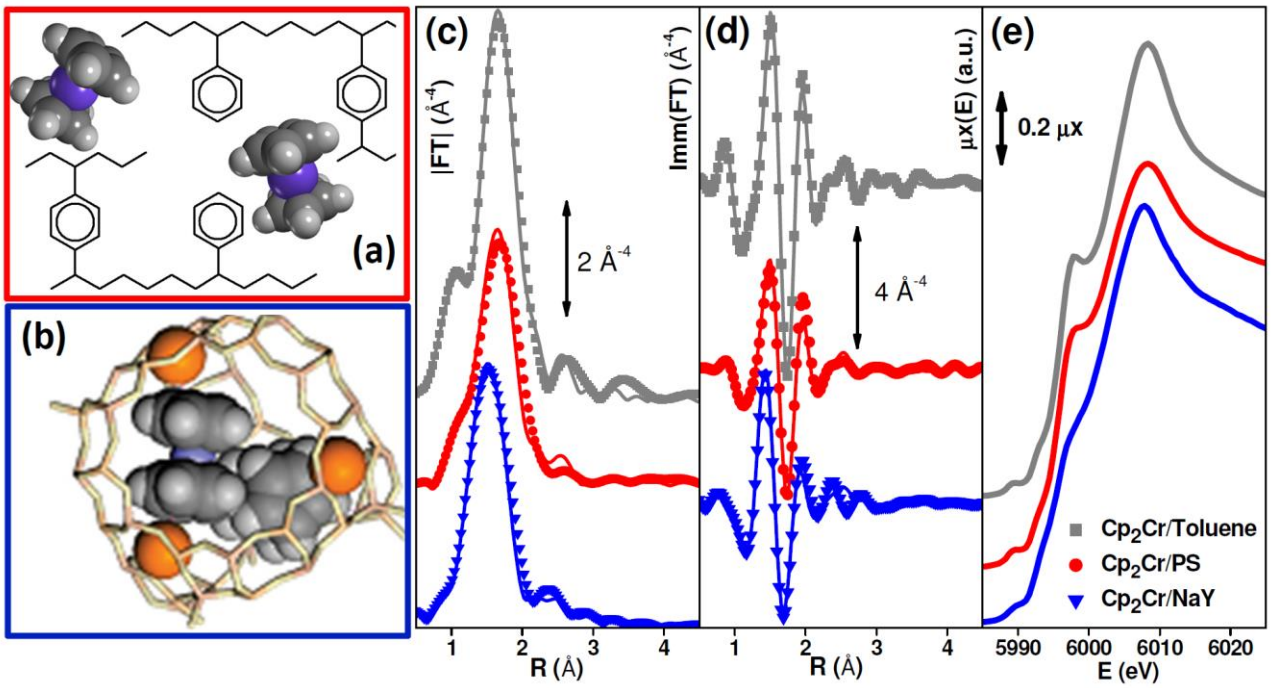

Figure 6. Part (a): Two Cp_2Cr molecules, reported as Corey-Pauling-Koltun (CPK) spheres: violet, dark grey, and light grey for Cr, C and H atoms respectively, encapsulated inside a 2D portion of PS matrix. Part (b) as part (a) where the Cp_2Cr molecules are encapsulated in a 3D portion of a zeolite cell (supercage cavity [84]); framework atoms are represented in the stick mode (Si and Al, light orange; O, light yellow) and Na^+ cations as orange CPK spheres. Part (c): modulus (a) of the k^3-weighted, phase-uncorrected, FT of EXAFS signals for Cp_2Cr/toluene (top grey curves), Cp_2Cr/PS (middle black curves), and Cp_2Cr/Na-Y (bottom blue curves experimental data as square dots and best fits as full lines). Part (d) as part (c) for the imaginary parts. Part (e) corresponding XANES spectra. Unpublished figure reporting data published in Ref. [37].

For both matrices, the absence of clustered Cp_2Cr molecules was determined by XAFS measurements. Results were compared with those obtained on Cp_2Cr in toluene solution (assumed as model for isolated molecules). From the k^3-weighted, phase-uncorrected Fourier transform (FT) of the EXAFS signals reported in Figure 6c,d (modulus and imaginary part) it is clearly evident that they are very similar. In fact they present a first-shell contribution around 1.6 Å due to 10 Cr-C SS paths and some MS contributions at higher distances but they do not show any other peak assignable to a Cr-Cr path characteristic for clusters of Chromocene molecules. Also the three XANES spectra (see Section 4.2 for a more detailed description) exhibit basically the same features confirming that the molecules are really isolated (Figure 6e). However, if we concentrate on the numerical results of the best fit for the three systems (Table 1), in the case of Cp_2Cr/Na-Y the molecule seems to be slightly distorted in fact we obtain a shorter mean distance $<r_{Cr\text{-}C}>$ resulting in a shift to shorter R values in FT of the EXAFS signal. The higher value of σ^2 Debye-Waller factor and the features less defined in the corresponding XANES spectrum indicate an higher heterogeneity of the species. This is assigned to different local electric fields experienced by Cp_2Cr molecules due to different statistical cation distribution in the supercages [84], see Figure 6b.

Table 1. Summary of the structural parameters optimized in the fit of the EXAFS data for the Cp_2Cr/toluene, Cp_2Cr/PS and Cp_2Cr/Na-Y systems. The fits run in R-space, in the 1.0-4.5 Å range. Single S_0^2 and ΔE_0 have been optimized for all SS and MS paths.

	Cp_2Cr/toluene	Cp_2Cr/PS	Cp_2Cr/Na-Y
S_0^2	0.7 ± 0.1	0.7	0.9 ± 0.1
ΔE_0 (eV)	0 ± 1	+1 ± 1	-4 ± 2
$<r_{Cr-C}>$ (Å)	2.169 ± 0.006 (DFT 2.201)	2.165 ± 0.008	2.11 ± 0.01
σ^2_{Cr-Cp} (Å^2)	0.003 ± 0.001	0.0070 ± 0.0005	0.010 ± 0.002
n° variables	4	3	4
R_{factor}	0.020	0.037	0.057

4.2. Determination of the electronic structure of Cp_2Cr by combined UV-Vis and XANES spectroscopies

In the same work, Estephane et al. [37] also reported a didactically instructive approach to determine the electronic structure of Cp_2Cr molecule based on the combination of UV-Vis and XANES spectroscopies.

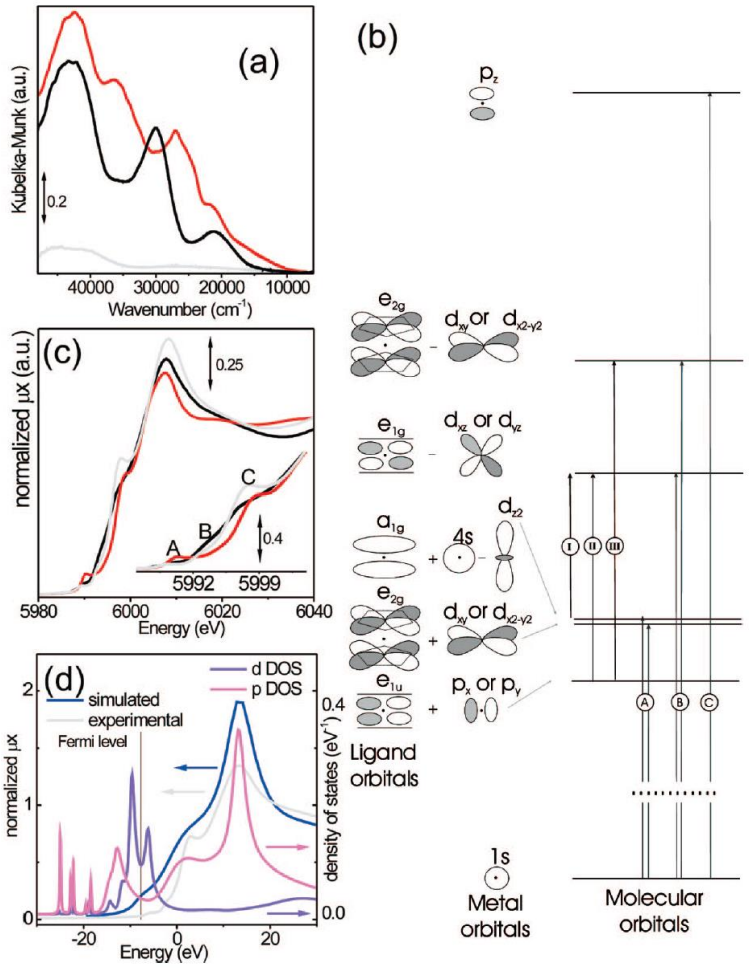

Figure 7. Part (a): UV-Vis DRS spectra of Cp_2Cr/Na-Y before (black line) and after (red line) CO dosage (equilibrium pressure P_{CO}= 150 Torr). Also the spectrum of Na-Y zeolite (gray line) is reported for comparison. Part (b): rough representation of the electronic transitions and the molecular orbitals involved in the electronic transitions responsible of the UV-Vis and XANES spectra. Part (c): XANES spectra of Cp_2Cr/Na-Y before (black line) and after (red line) CO dosage (equilibrium pressure P_{CO}= 150 Torr). Also the spectrum of Cp_2Cr in toluene is reported for comparison (light gray). The inset reports a magnification of the pre-edge region. Part (d), left ordinate axis: simulated XANES spectrum of Cp_2Cr (blue) compared to experimental one for Cp_2Cr in toluene (light gray, horizontally translated to match the white line position). Right ordinate axis (as indicated by the arrows) shows the *p* and *d* projected DOS for the Cr atom (magenta and violet, respectively). Reproduced with permission from Ref. [37], copyright American Chemical Society (2009).

When Cp_2Cr is sublimed onto the Na-Y powder, the white zeolite acquires a light salmon color. As a consequence, the UV-Vis spectrum of Cp_2Cr/Na-Y system (Figure 7a, gray curve) is characterized by three main components centered around 21000, 30000 (responsible for the color) and 43000 cm^{-1} (henceforth labeled as components **I**, **II** and **III**, respectively). These bands are very similar to those observed in the spectrum of chromocene in solution [85,86]. A simplified scheme of the electronic structure of Cp_2Cr is reported in Figure 7b. In the idealized D_{5d} symmetry, the 10 π orbitals of the two Cp rings form the symmetry adapted combinations a_{1g}, a_{2u}, e_{1g}, e_{1u}, e_{2g} and e_{2u}. Interaction of these ligand-centered orbitals with the metal 3*d*, 4*s* and 4*p* valence atomic orbitals of appropriate symmetry generates the molecular orbitals shown in the right side of the diagram.

The Cp_2Cr ground state is $^3E_{2g}$, resulting from the $e_{2g}^3\, a_{1g}^1$ configuration [85]. The transitions of one of the 16 valence electrons into a non-occupied molecular orbital are responsible for the observed optical spectrum (Figure 7a). Only the lowest frequency component (21000 cm^{-1}) has been definitely assigned in literature in terms of a *d*-*d* transition ($^3E_{2g} \rightarrow {}^3E_{1g}$, $^3E_{2g}$, $^3A_{1g}$, $^3A_{2g}$). Based on this, band **I** is due to an electronic transition from the HOMO to the LUMO [87-89]. The *d*-*d* character of transition **I** is easily explained by considering that both the HOMO and the LUMO are primarily metal in character ($d_{xy,x2-y2}$ for the HOMO and $d_{xz,yz}$ for the LUMO) [90]. The bands at 30000 and 43000 cm^{-1} were assigned to ligand-to-metal charge transfer transitions [37]. The key feature from this investigation is that the UV-Vis spectrum of Cp_2Cr/Na-Y clearly indicates that Cp_2Cr is simply encapsulated as neutral Cp_2Cr molecule inside the supercages of Na-Y zeolite and no further reaction occurs, since similar spectra have already been reported for chromocene in solution [85,86] and in a frozen argon matrix [91].

Estephane et al. [37] used the same simplified scheme also to understand the Cr K-edge normalized XANES spectrum of Cp_2Cr, in the approximation that the core hole generated in the Cr(1*s*) orbital by the X-ray absorption does not strongly perturb the molecular levels. The XANES spectrum of Cp_2Cr in Na-Y zeolite (black curve in Figure 7c), is compared to that of Cp_2Cr in toluene solution (solid gray curve).

The spectrum of the reference sample is characterized by three main features in the pre-edge region at 5989.2, 5992.8 and 5997.7 eV (labeled **A**, **B** and **C**, respectively), followed by an intense and sharp white-line centered at 6008.2 eV. To allow an assignment of these features described above, the authors have performed a simulation of the XANES spectrum of the Cp_2Cr molecule with FEFF8.4 code [92,93]. Figure 7d compares the simulated XANES spectrum of the isolated molecule (blue) with the experimental one collected in toluene solution (light gray), properly translated to match the energy position of the white-line transition. The simulated spectrum is in a good agreement with the experimental one and is able to reproduce the energy position and the relative intensity of all the features. In Figure 7d (right ordinate axis) are also reported, on the same energy scale, the calculated projected DOS for the Cr atom. Comparison of the simulated spectrum with the projected DOS allows the assignment of the main XANES features, that can be divided in two families. At lower energy, features **A** and **B** are due to the transition between 1*s* orbital and Cr levels characterized by a significant *p*/*d* hybridization. At higher energy, C and white-line features are due to the transition of a 1s electron into almost "pure" *p* levels. On the basis of this simulation, the intense **C** feature is assigned to the dipole-allowed $1s \rightarrow 4p_z$ transition (see the electronic scheme reported in Figure 7b) and is consequently very sensitive to coordination and geometry variation along the z axis of the molecule [94]. For a complete assignment of features **A** and **B**, a combination of XANES (Figure 7c) and UV-Vis (Figure 7a) spectra is mandatory. The energy difference between the levels originated from the $e_{1g} - d_{xz},d_{yz}$ (LUMO) and $e_{2g} - d_{xy},d_{x2-y2}$ anti-bonding combinations is, from UV-Vis spectrum (frequency difference between band **III** and band **II**), 13000 cm^{-1} (1.6 eV), a value too narrow to be resolved in the XANES spectrum owing to the core-hole broadening. The shoulder **B** is consequently assigned to the unresolved electronic transitions from 1*s* to these levels. Finally, the **A** feature, found 3.6 eV (29000 cm^{-1}) below **B**, is assigned to the dipole-forbidden transitions from the 1*s* to the HOMO levels. In fact, the UV-Vis spectrum reveals that the almost degenerated and partially unoccupied HOMO levels lie 21000 cm^{-1} below

the LUMO level and 34000 cm^{-1} below the levels originated from the $e_{2g} - d_{xy},d_{x2-y2}$ anti-bonding combinations, respectively (average value of 27500 cm^{-1}, as XANES does not resolve the two final states).

The XANES spectrum of the Cp_2Cr/Na-Y system presents basically the same main features discussed so far for Cp_2Cr in toluene, corroborating the conclusion of the UV-Vis study, i.e. that Cp_2Cr is confined in the Na-Y super-cages without changes of the Cr oxidation state. However, the spectrum is less resolved, indicating a higher heterogeneity of species. This is assigned to different local electric fields experienced by Cp_2Cr molecules, due to different statistical cation distribution in the super-cages of the Y zeolite. In further detail, feature **A** remains basically unchanged, feature **B** increases in intensity, while an inverse behavior is observed for both feature **C** and for the white line. As the most affected feature is the **C** one, XANES data evidenced an appreciable structural modification of the Cp_2Cr molecule along the z axis, due to the interaction with the zeolitic walls and to the presence of strong local electric fields [95].

4.3. Reactivity of Cp_2Cr hosted in PS and in Na-Y zeolite towards CO: IR and XAFS results.

Estephane et al. [37] followed the interaction of CO with both Cp_2Cr/PS and Cp_2Cr/Na-Y matrix system with IR spectroscopy. In the case of PS the formation of a time-stable $Cp_2Cr\cdots CO$ monocarbonyl complex was demonstrated, in fact upon dosing CO at RT on the Cp_2Cr/PS system, an intense band at 1900 cm^{-1} appears in the FTIR spectrum (Figure 8a), assigned to the ν(CO) of the $Cp_2Cr(CO)$ complex. This band was previously observed in literature for direct addition of CO to a toluene solution but the complex formed was labile [80], so the improvement by working with a "solid solvent" matrix is clearly evident. In a successive work, Estephane et al. [83] used the EXAFS spectrum of the $Cp_2Cr(CO)$ complex formed inside the PS matrix to validate the ab initio models predicting a triplet → singlet spin transition in the $Cp_2Cr(CO)$ +CO → $Cp_2Cr(CO)$ reaction.

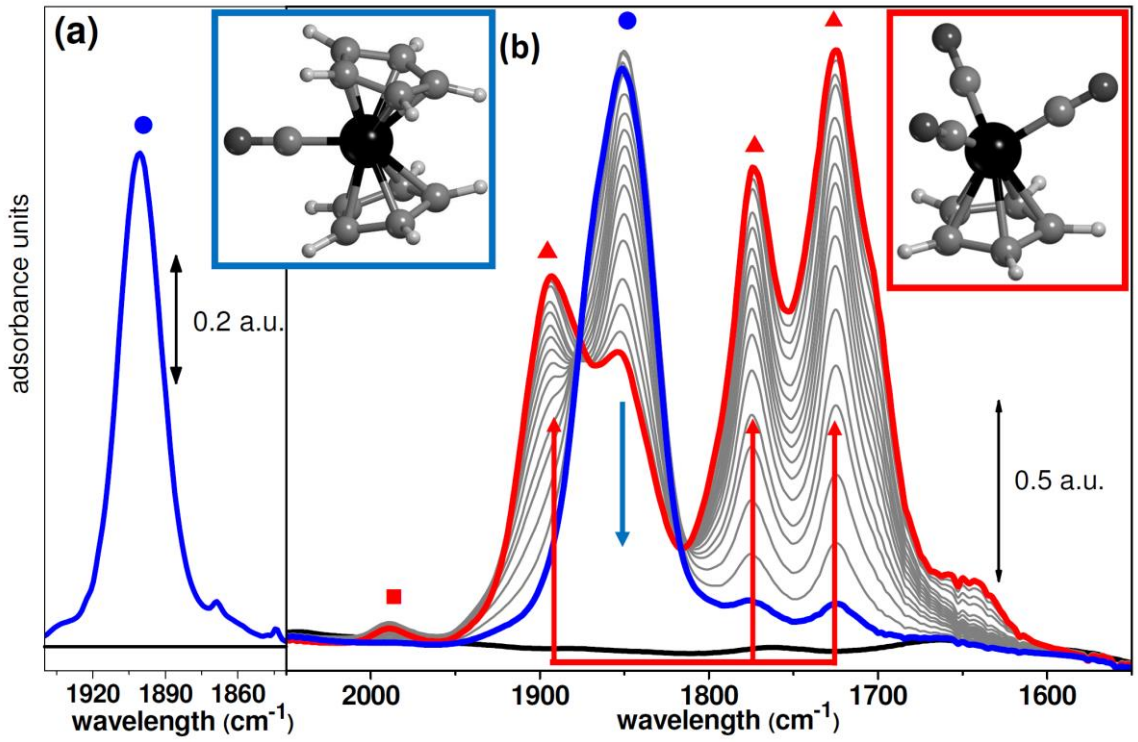

Figure 8. Part (a): FTIR spectra collected at RT on the Cp_2Cr/PS system before (black) and after (blue) dosage of C. No time evolution is observed in this experiment. Part (b): FTIR spectra collected at RT on the Cp_2Cr/Na-Y system before (black), immediately after dosage of CO (blue), after 1 h (red) and intermediate times (grey curves). The blue inset reports the structure of the $Cp_2Cr(CO)$ complex responsible of the IR band at 1900 cm^{-1} (PS) or at 1850 cm^{-1} (Na-Y). The red inset reports the structure of the $[CpCr(CO)_3]^-$, complex responsible of the IR triplet at 1893, 1773 and 1724 cm^{-1}. Unpublished Figure reporting data published in Ref. [37].

The case of Na-Y is more complex as it presents a rapid evolution in time. Upon CO addition the Cp_2Cr/Na-Y system in the FTIR spectrum an intense band in the ν(CO) region at 1850 cm^{-1} immediately appears (bold blue curve in Figure 8b), and can be assigned to a monocarbonyl complex of the type $Cp_2Cr(CO)$. The red-shift of the value with respect to PS was explained by high ionic environment [37]. By waiting in time this band is progressively eroded and simultaneous three bands at 1893, 1773 and 1724 cm^{-1} (red triangles in Figure 8b) appears accompanied by a weak component at ~1980 cm^{-1} (red square) growing in a similar way. The evolution was interpreted in terms of an evolution of the monocarbonyl precursor into a tricarbonyl charged species $[CpCr(CO)_3]^-$, after the loss of a Cp ring. This transformation being favored by the intense electric field present inside the zeolite's cavities. In the same way the weak component at ~1980 cm^{-1} was assigned to a fraction of $[Cp_2Cr(CO)]^+$ species [37].

k^3-weighted FT of the EXAFS data and XANES spectra (Figure 9a,b) reflect the behavior observed by IR and highlight structural variations undergone by the Cp_2Cr molecule upon CO addition. In particular, for the Cp_2Cr/PS system, the modulus (top spectra in Figure 9a) exhibits an increase of the intensity and a shift toward higher R values of the first shell, and together with the numerical results of the good fit (made starting from ab initio models of a monocarbonyl specie) prove the insertion of a CO ligand and a consequent rearrangement of the Cp rings with elongation of the average $<r_{Cr-C}>$. It appears also an additional high R component, centered around 2.5 Å but with different phase with respect to Cr-Cp MS (see imaginary part Figure 9a), that is ascribed to the strong collinear Cr-C-O MS contributions. In a similar way the modification of all the pre-edge XANES features, confirm that the Cp_2Cr molecules loose their symmetry and undergo a relevant distortion after interaction with CO, see Figure 9b.

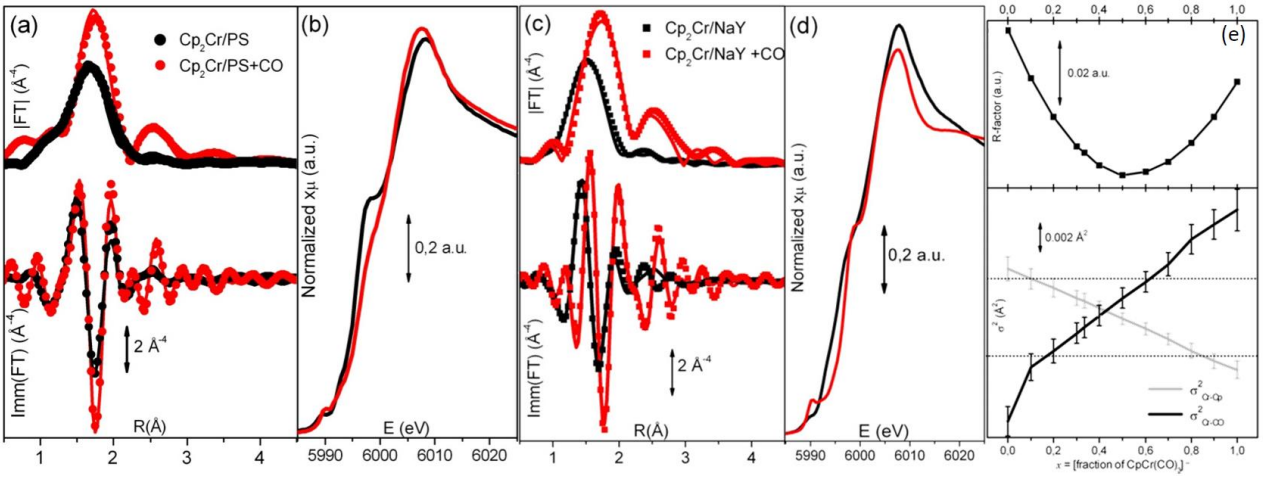

Figure 9. part (a): Modulus (top) and imaginary part (bottom) of the k^3-weighted, phase uncorrected, FT of the EXAFS spectra of the Cp_2Cr/PS systems before (black curves) and after (red curves) CO dosage. The experimental data (scattered) are superimposed with the best fit (full lines). Part (b): as part (a) for the XANES spectra. Parts (c) and (d): as parts (a) and (b) for the Cp_2Cr/Na-Y system. Part (e): Results of the two phases fit on Cp_2Cr/Na-Y + CO system trend of R-factor and of Debye-Waller factors in function of the relative percentage of products of reaction. Unpublished Figure reporting data published in Ref. [37].

In Cp_2Cr/Na-Y system, XANES spectrum upon CO addition shows a white line intensity strongly modified and pre-edge features better resolved, suggesting a better molecular definition of the Cr species formed upon CO contact. The $[CpCr(CO)_3]^-$ and $[Cp_2Cr(CO)]^+$ product species hypothesized from the IR study could justify this behaviour even if the position of the edge is almost unaltered and the two product should be characterized by a different formal oxidation state, but is possible that the charges are delocalized across the entire molecule and not localized on the Cr centre.

Combining indications obtained by previous techniques with quantum mechanical calculation we simulated the EXAFS signal of the possible products of reaction between Cp_2Cr/NaY and CO. Because the time of CO contact in the XAS experiment is much longer than that of IR, the initial

species $Cp_2Cr(CO)$ is not expected to be detected by this technique, while only the final state with the copresence of the $[CpCr(CO)_3]^-$ and $[Cp_2Cr\text{-}(CO)]^+$ species is expected to be observed. We initially performed two separate fits by supposing the presence of only one of the two species but both of them gave numerical results physically unreliable (underlined values in Table 2). Therefore we tried to quantitatively evaluate their relative amounts by means of a two phases fit

Table 2. Summary of the structural parameters optimized in the fitting of the EXAFS data for the Cp_2Cr/Na-Y + CO systems. The fits were performed in R-space in the 1.0-4.5 Å range. Not optimized parameters are recognizable by the absence of the corresponding error bars. Underlined parameters evidences mathematical values of the fit that are physically not acceptable.

	1 phase $[CpCr(CO)_3]^-$	1 phase $[Cp_2Cr(CO)]^+$	2 phases $[CpCr(CO)_3]^-$	2 phases $[Cp_2Cr(CO)]^+$
S_0^2	0.9 ± 0.2	<u>0.6 ± 0.1</u>	0.9**x*	0.9*(1-*x*)
ΔE_0 (eV)	1 ± 2	1 ± 2	3 ± 1	
$<r_{Cr\text{-}C}>$ (Å)	2.193 ± 0.009	2.20 ± 0.01	2.227 ± 0.006	2.196 ± 0.006
$\sigma^2_{Cr\text{-}Cp}$ (Å^2)	<u>0.001± 0.001</u>	0.004 ± 0.002	0.0047 ± 0.0006	
$<r_{Cr\text{-}CO}>$ (Å)	1.82 ± 0.02	1.85 ± 0.01	1.822 ± 0.006	1.893 ± 0.006
$\sigma^2_{Cr\text{-}CO}$ (Å^2)	<u>0.012 ± 0.002</u>	<u>0.000 ± 0.001</u>	0.006 ± 0.001	
n° variables	6	6	6	
R_{factor}	0.046	0.035	0.013	

A phase fraction parameter *x* has been added to the fit, weighting the signals of the species $[CpCr(CO)_3]^-$ and $[Cp_2Cr(CO)]^+$ by *x* and (1–*x*), respectively. Other parameters have been constrained in order to keep fixed the same number of variables optimized to 6, as for the two previous fits, so that they are directly comparable. The good quality of the fit is further appreciable in Figure 9c, and looking to the results, the R_{factor} is significantly improved and, more importantly, enforcing *x* value to move from 0 to 1 with 0.1 step all optimized parameters now lie within the physical acceptable ranges for in the 0.3–0.6 interval. Being the phase fraction parameter *x* optimized to 0.50±0.07, as confirmed by the minimum in the R-factor trend in function of *x* in Figure 9e, Esptephane et al. concluded that the two species are almost equi-populated [37].

Summarizing, PS and Na-Y zeolite matrices can both act as "solid solvent" for the Chromocene molecules, thus permitting the study of their interactions with simple reagents sent into the matrices in gas phase (operation that is much more difficult in the case of a liquid solution). The differences between the two matrices are reflected on the molecules encaged, slightly in term of geometry but especially in term of their reactivity. In fact, interaction of Cp_2Cr with CO in PS comports the addition of only one CO, while in the zeolite an higher, but also much more complex, reactivity is observed giving as product new charged complexes not only monocarbonyls but also $[CpCr(CO)_3]^-$ where one Cp substituted by three CO molecules.

5. Organometallic complexes in solution: the cis-$[Ru(bpy)_2(py)_2]^{2+}$ case study

The structure of an organometallic complex is influenced by its ligands, so some difference are expected moving from the crystalline phase to the dispersed phase either in different solvents or after grafting on different high surface area supports. As relevant applications required dispersed organometallic complex, the knowledge of such structures can be very important. As diffraction techniques can not be applied in such conditions, scientists uses theoretical (ab initio) and spectroscopic approaches. For the latter we will focus on EXAFS in the following.

On the methodological ground, the procedure hereinafter reported for *cis*-$[Ru(bpy)_2(py)_2]^{2+}$, is based on the use of DFT-optimized geometries as initial guess for the EXAFS fit, can be easily transposed to the analysis of others metallorganic complexes. Beside the validation of DFT-geometries, the analysis discussed in this Section can be regarded as an example-case of EXAFS

refinement in complex metallorganic systems. Here, a careful path selection and grouping is fundamental to correctly model the EXAFS signal, and allows to extract the maximum information level from EXAFS characterization. Section 5.1 discuss the results of the structural refinement in a more discursive approach, while Section 5.2 treat the same matter in a more technical and advanced way and can be skipped by beginners.

5.1. Structure refinement of cis-$[Ru(bpy)_2(py)_2]^{2+}$ in aqueous solution by EXAFS spectroscopy

Due to the complexity of the structure, more than 200 single scattering (SS) and multiple scattering (MS) paths were generated by the FEFF code. 30 main paths were selected, according to the criteria discussed in details in the Section 5.2. These paths were sufficient to properly reconstruct the overall EXAFS signal.

To limit the number of optimized variables, all paths were optimized with the same amplitude factor (S_0^2) and with the same energy shift (ΔE) parameter. Moreover, both the two pyridine (py) and two bpyridine (bpy) ligands were considered as rigid molecules, whose only degree of freedom is the radial translation along the corresponding Ru–N axis. The two pairs of py and bpy ligands were assumed to behave in the same way, respectively. Consequently, the only two structural parameters optimized in the fit were the distances $R_{Ru–N(py)}$ and $R_{Ru–N(bpy)}$; the lengths of all the other paths were calculated starting from these two values, according to geometrical constraints imposed by the rigidity of the py and bpy units.

Concerning the Debye-Waller (DW) factors, only two parameters were optimized: $\sigma_{Ru–N(py)}$ and $\sigma_{Ru–N(bpy)}$, associated with Ru–N bonds for py or bpy ligands, respectively. DW factors for SS and MS paths involving atoms of the same ligand are modeled as $\sigma^2 = \sigma^2_{Ru–N(L)}(R_{eff}/R_{Ru–N(L)})^{1/2}$ (where L = py or bpy and R_{eff} is the mean free length of the path). In such a way, when R_{eff} increases, the expected proportional expansion of its standard deviation (σ) is roughly accounted. Several almost co-linear MS paths involve two N atoms of two opposite L and L' ligands: correspondent DW factors were computed as $\sigma^2_{MS} = \sigma_{Ru–N(L)}{}^2 + \sigma_{Ru–N(L')}{}^2$.

Summarizing, the fit runs over 6 independent parameters only. A similar approach to validate a complex structure by EXAFS (previously refined by XRD of the crystalline phase or optimized *via* DFT-calculations), maintaining a limited number of optimized parameters, has successfully employed in the similar case of the $[Ru(bpy)_n(AP)_{6–2n}]Cl_2$ (AP = 4-aminopyridine, n = 1, 2, 3) complex by Salassa et al. [96], or of Cp_2Cr hosted in different porous matrices by Estephane et al. [37,83] (and here discussed in Section 4), or for metal organic frameworks by Bonino et al. [97].

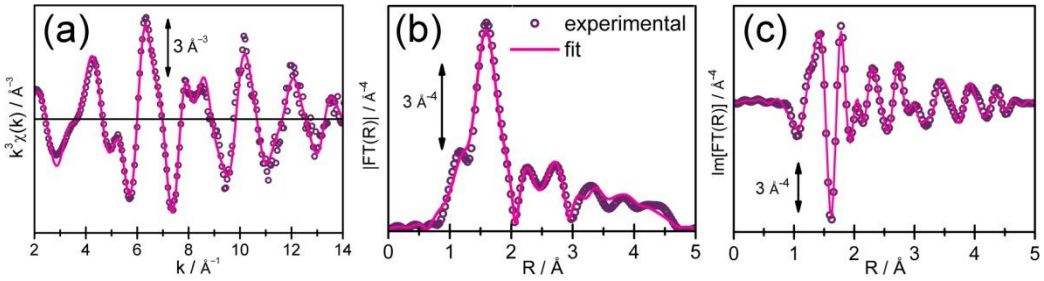

Figure 10. (a) Experimental $k^3\chi(k)$ EXAFS spectrum of *cis*-$[Ru(bpy)_2(py)_2]^{2+}$ (violet curve) compared with its best fit (magenta curve). Corresponding phase-uncorrected FT modulus (b) and (c) imaginary part. Optimized parameters of the fit are reported in Table 3.

The quality of the obtained fit in both R- and k-spaces can be appreciated in Figure 10 and is further confirmed by the very low values of both R-factor and errors associated to the fitting parameters (see Table 3). It is worth highlighting that bpy units contribute to the high-distance paths almost twice as much as the py units. Consequently, distances and DW factors were determined with a better precision for the bpy ligands. Accordingly to the lower mass, py units exhibit a DW factor higher than bpy. The nitrogen atom of the py units is located at a distance of 2.09 ± 0.01 Å from Ru, hence 0.08 Å shorter than the value predicted by DFT calculations (Table 3). Also the experimental Ru–N(bpy) distances are 0.03 Å shorter than the theoretical ones. Interestingly, the

optimized $R_{Ru–N(bpy)}$ and $R_{Ru–N(py)}$ distances become equivalent taking account of the associated errors. Such a trend is characteristic of the EXAFS technique, in particular dealing with structures where several neighbor atoms of the same chemical nature are located at close distances. Here, a tendency towards equalization of the refined bond distances is commonly observed [37,83,97-99]. In conclusion, EXAFS data analysis fully confirms the overall structure optimized in the DFT calculations. Furthermore, the results reported in Table 3 are in good agreement with previous studies performed on similar ruthenium complexes [96,98,99].

Table 3. Summary of the optimized parameters in the EXAFS data fitting (Figure 10). The fits were performed in R-space in the 1.0–5.0 Å range over k^3-weighted FT of the $\chi(k)$ functions performed in the 2.0–14.0 $Å^{-1}$ interval. A single ΔE and a single S_0^2 were optimized for all SS and MS paths. Optimized bond distances are compared to the average values obtained from DFT calculations.

EXAFS fit parameters for *cis*-$[Ru(bpy)_2(py)_2]^{2+}$ with comparison to DFT calculations		
Parameter	EXAFS	DFT optimization
N_{ind}	30	–
N_{fit}	6	–
R_{factor}	0.032	–
S_0^2	0.72 ± 0.05	–
ΔE (eV)	2.5 ± 0.6	–
$R_{Ru–N(bpy)}$ (Å)	2.073 ± 0.007	2.11
$\sigma_{Ru–N(bpy)}$ ($Å^2$)	0.0027 ± 0.0006	–
$R_{Ru–N(py)}$ (Å)	2.09 ± 0.01	2.17
$\sigma_{Ru–N(py)}$ ($Å^2$)	0.004 ± 0.001	–

5.2. Advanced details on the EXAFS structure refinement of cis-$[Ru(bpy)_2(py)_2]^{2+}$ complex

In the EXAFS data, both $k^3\chi(k)$ function and its Fourier Transform in the R-space clearly show a structured signal which reflects the structural complexity of the investigated Ru-complex. As previously mentioned, the DFT-optimized geometry was used as input for FEFF8.4 code, to perform the EXAFS data analysis. Considering that all the atoms of the complex are comprised in an ideal sphere of radius ~ 5 Å, centered on the Ru atom, the calculation was limited to SS and MS paths with less than four legs and R_{eff} < 5 Å. In this way, more than 200 different paths, with their relative amplitudes and phases, were obtained.

Such a high number of paths is due to the low symmetry of the computed structure (geometry optimization performed without symmetry constraint). Indeed, every single path that would be obtained with a perfectly symmetric model is actually split into several slightly different paths (R_{eff} variations in the order of ± 0.01 Å), due to the loss of degeneracy.

Therefore, a significant decrease in the overall number of EXAFS paths can be first obtained by re-grouping together the split paths, involving atoms in quasi-symmetric positions of the molecule. Additionally, a further reduction of the number of considered paths is achieved by excluding those having an amplitude smaller than 10% of the most intense path (the Ru–N(bpy) SS path, corresponding to the N of the closest bpy unit located at ca. 2.11 Å). Hence, only 30 of the initial 200 SS and MS paths are effectively employed to model the experimental EXAFS spectrum of *cis*-$[Ru(bpy)_2(py)_2]^{2+}$.

Hereinafter, the specific contribution of the selected scattering paths to the overall EXAFS signal will be discussed. All paths shown below were computed using the values S_0^2, ΔE, $R_{Ru–N(bpy)}$, $\sigma_{Ru–N(bpy)}$, $R_{Ru–N(py)}$, $\sigma_{Ru–N(py)}$ obtained from the best fit, reported in Table 3. Looking at the experimental data (see Figure 10b), three well-defined contributions localized in different regions of the R-space can be individuated, in particular in the 0.75–2.05 Å, 2.05–3.00 Å and 3.00–4.75 Å ranges. The first interval contains the first-shell Ru–N SS paths of the four ligands (4- and 2-fold degenerate contributions from bpy and py respectively, light blue curve in Figure 11a,b).

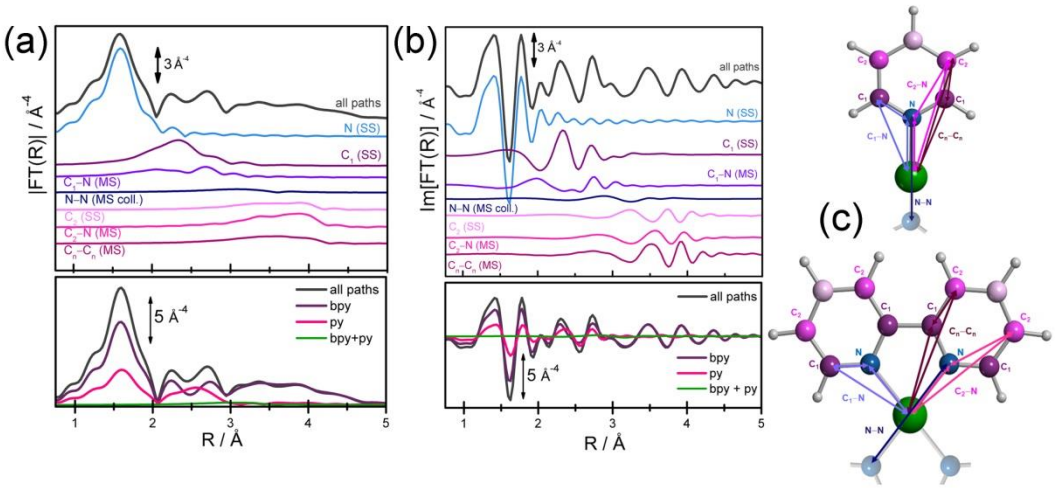

Figure 11. Different path contributions to the overall EXAFS signal of the cis-$[Ru(bpy)_2(py)_2]^{2+}$ complex. Part (a) moduli and part (b) imaginary parts of the phase uncorrected FT. All path contributions were computed using for the parameters the values obtained from the best fit (see Table 3). The bottom panels show the moduli and imaginary parts (in (a) and (b), respectively) of the phase uncorrected FT relative to the three subsets of paths involving exclusively atoms either of the bpy (purple line) or py ligands (magenta line), or mixed paths involving atoms of both ligand types. (c) Structure of py and bpy ligands indicating the atoms involved in the EXAFS paths, and the paths themselves using same color code of part (a).

In the 2.05–3.00 Å range, the Ru–C_1 SS and the Ru–C_1–N MS paths contribute (purple and violet lines in Figure 11a,b) with the following degenerations relative to bpy and py: 8 and 4 for the SS, 16 and 8 for the MS. In the MS case, the number of equivalent paths is doubled with respect to SS because the amplitude, phase and total length remain unchanged reversing the order of the atoms involved in the scattering process (Ru–C_1–N ≡ Ru–N–C_1). In the last region, corresponding to higher R-values, the Ru–C_2 SS (light pink curve in Figure 11a,b, degenerated over 12 atoms, 8 belonging to bpy and 4 to py) and other MS paths are present. These involve a C_2 atom with one or more atoms among N (magenta curve), C_1 or a different C_2 (dark pink curves in Figure 11a,b). Furthermore, a Ru–N–N MS collinear path (degeneration 6, dark blue line in Figure 11a,b) is present, which involves three pairs of N atoms in mirror position with respect to the central Ru atom.

Alternatively, the paths can also be grouped in three subsets, depending on the ligand to which each scatterer atom belongs: (i) bpy ligands only, (ii) py ligands only, (iii) both bpy and py ligands. The bottom panels in Figure 11 reports in R-space (both modulus, panel (a), and imaginary part, panel (b)) the sum of the paths belonging to the three subsets as purple, dark pink, and green curves, respectively. The sum over all the paths, including type-(i), -(ii) and -(iii) signals, is also shown for comparison (gray curve).

From the analysis of the paths contribution distinguishing on the ligand-type, the following important information emerges:

- the overall contribution of bpy paths (i) is higher than that due to py paths (ii), in agreement with the higher number of atoms contributing to the scattering process;
- the mixed contribution involving atoms of both bpy and py ligands (iii) is limited to one Ru–N–N MS collinear path, 2-fold degenerated, and can be neglected;
- in the higher R-values interval (3.00–4.75 Å), the ratio between signal amplitude of (i) and (ii) shows a remarkable change. The 2:1 ratio present in the smaller-R intervals now becomes notably higher. This could be explained considering that for the bpy units more MS paths are possible, since the atoms of two different rings linked together are involved. Furthermore, the bidentate nature of the bpy ligand is such that the Ru–N–C_2 angles are closer to 180° with respect to the same angles in the py ligand (see Figure 11c), and consequently the corresponding paths are closer to collinearity.

6. EXAFS study on MOFs of the UiO-66/UiO-67 family: comparison with XRPD and ab initio investigations

The recently discovered UiO-66/67/68 class of isostructural MOFs [100] has attracted great interest because of its remarkable stability at high temperatures, high pressures and in presence of different solvents acids and bases [101].

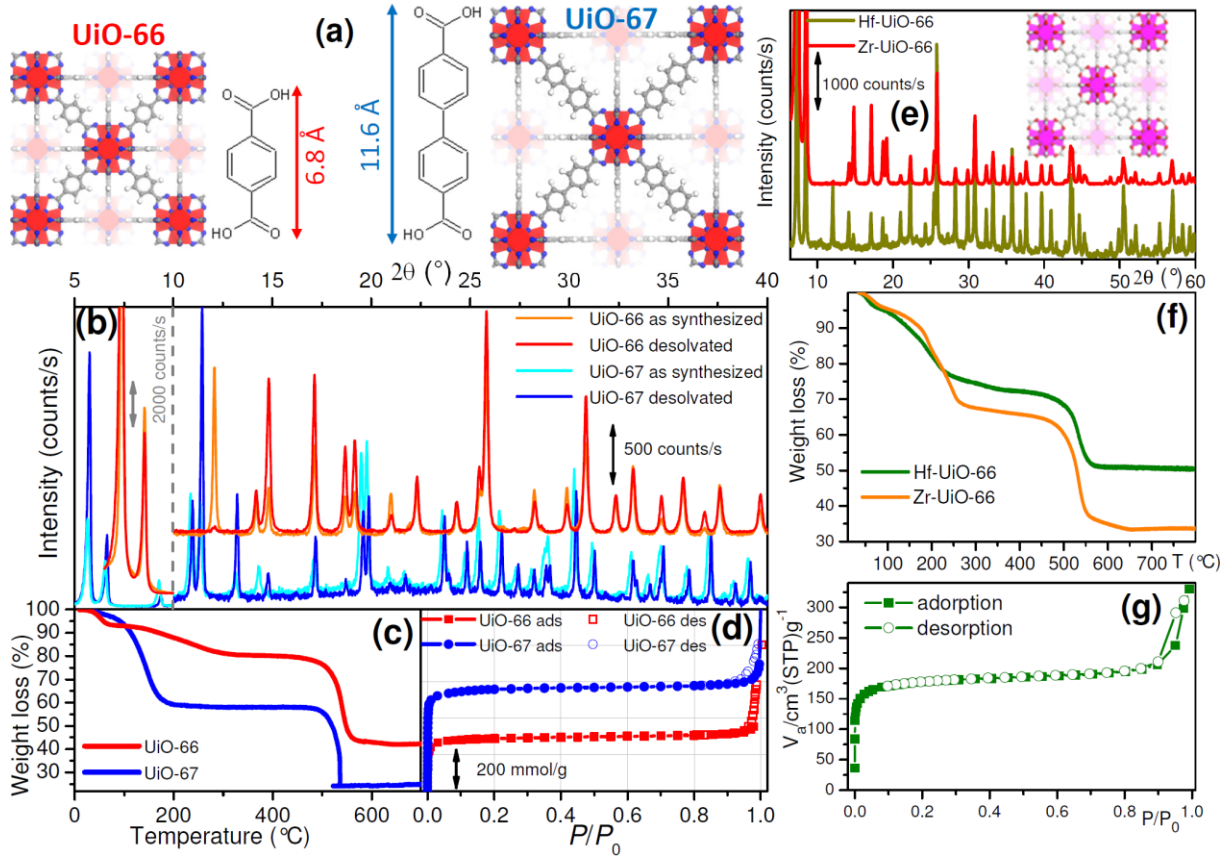

Figure 12. Part (a): From left to right: comparison of the dimension of linker, structure, for the isostructural UiO-66 and UiO-67 MOFs. Part (b): Comparison of the XRPD patterns (λ=1.540 Å) for as prepared UiO-66 (UiO-67), orange (cyan) curve and activated at 300 °C (red and blue curves). The patterns in the 10-40 2θ ° region have been amplified by a factor 4. Patterns related to UiO-66 have been vertically translated for clarity. Part (c): TGA curve of UiO-67 and UiO-67 samples, red and blue curves, respectively. In both cases, the heating ramp was of 5 C/min in a N_2 flow (100ml/min). Part (d): volumetric N_2 adsorption isotherms recorded at 77 K on UiO-66 (red squares) and UiO-67 (blue circles). Empty and filled scatters refer to the adsorption and desorption branches, respectively. Part (e): XRPD pattern (λ=1.540 Å) of Hf-UiO-66 (green) and Zr-UiO-66 (red) in their solvated forms. The inset reports the MOF structure. Part (f) Weight loss of Hf-UiO-66 relative to the start mass (green curve). The weight loss of Zr-UiO-66 has been added as a reference (orange curve). Since hafnium is 41% heavier than zirconium, the Zr-UiO-66 shows both higher initial and breakdown losses. Part (g): N_2 adsorption/desorption isotherm for Hf-UiO-66 at 77 K. Unpublished figure reporting data from Refs. [100-102,104,105].

UiO-66 is obtained connecting $Zr_6O_4(OH)_4$ inorganic cornerstones with 1,4-benzene-dicarboxylate (BDC) as linker, while the isostructural UiO-67 material, obtained using the longer 4,4′ biphenyl-dicarboxylate (BPDC) linker [102] (Figure 12a) and Hf-UiO-66 is obtained keeping the UiO-66 linker (BDC) and substituting the $Zr_6O_4(OH)_4$ blocks with $Hf_6O_4(OH)_4$ corners (inset in Figure 12e). XRPD, see Figure 12b,e testifies the quality of the synthesis. Due to the rigidity of the framework several isostructural UiOs has been prepared and tasted for the stability and gas adsorption. Kandiah et al. [103] studied the thermal and chemical stabilities of isostructural UiO-66-X (X= NH_2, Br and NO_2) and observed the lower stability of this analogue with respect to parent UiO-66. Conversely, as documented by the thermogravimetry studies reported in Figure 12c,f UiO-67 [102] and Hf-UiO-66 [104] show thermal and chemical stability similar to that of UiO-66 and exhibit the expected surface area, as determined by low temperature volumetric N_2 adsorption

isotherms (Figure 12d,g). Such a high stability is related to the fact that each Zr- (Hf-) octahedron is 12-fold connected to adjacent octahedra. This connectivity is very common for metals, resulting in the highly packed fcc structure, but it is still almost unique in MOF topologies.

The desolvation process left almost unchanged the XRPD pattern of such materials (Figure 12b): besides a gain of intensity of the basal reflections (due to the removal of the electron density inside the pores) [106-108] all peaks remains in almost the same 2θ position with small intensity changes. Conversely, an huge modification of the EXAFS spectra is obtained in all cases, see Figure 13.

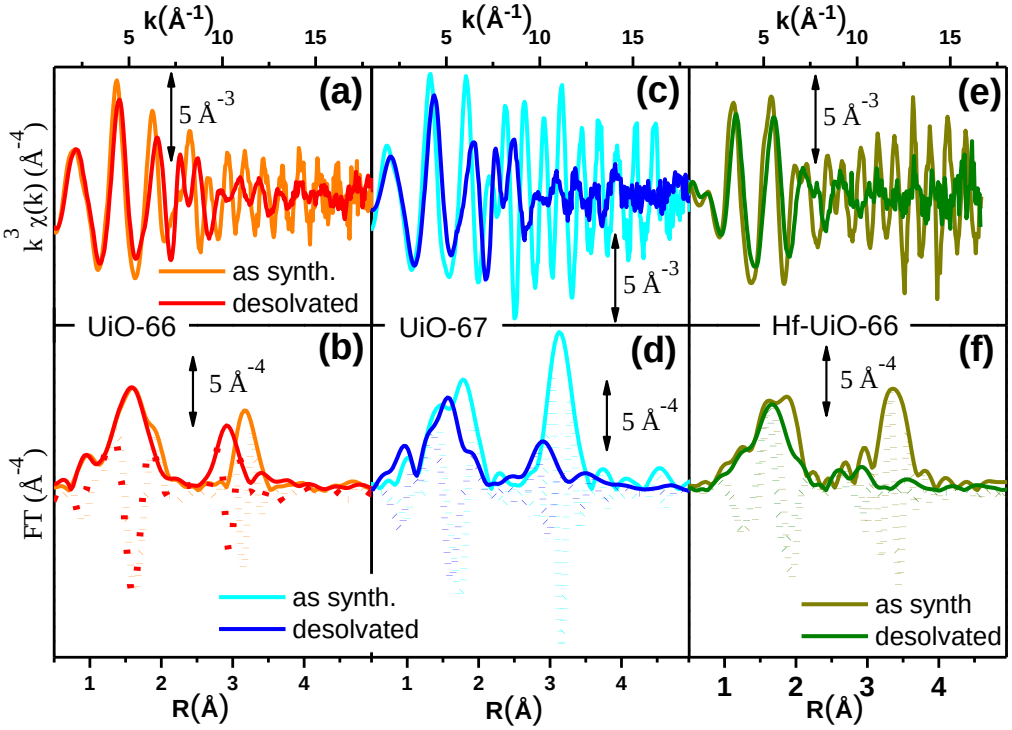

Figure 13. k- (top panels) and R-space (bottom panels) EXAFS data collected on UiO-66, UiO-67 and Hf-UiO-66, parts (a,b), (c,d) and (e,f), respectively. Both as synthesized (or hydroxylated) and desolvated (or dehydroxylated) forms of the three different isostructural MOFs have been measured. With the exception of desolvated Hf-UiO-66 sample (collected at 573 K) remaining spectra were collected at 300 K. Unpublished figure reporting data from Refs. [100-102,104,105].

In the three hydroxylated materials, the structure determined from the Rietveld refinement of the XRPD corresponding patterns resulted in a straightforward interpretation of the complex EXAFS signals, see first three columns in Table 4. The dramatic modification undergone by the EXAFS spectrum upon dehydroxylation (see Figure 13) makes the data analysis not so straightforward. In the case of UiO-66 (see Figure 13b, but similar effects are observed in the two other cases) the changes are basically explained in terms of three main effects: (i) small contraction of the first M-O shell (M = Zr or Hf) accompanied by a small decrease in coordination (erosion of the shoulder around 1.9 Å); (ii) relevant distortion of the second shell contribution showing a maximum that moves from 3.17 Å to 2.91 Å, with a shoulder at 3.41 Å, thus reflecting an important splitting of the R_{M1} distances of the octahedron sides; (iii) the almost complete disappearance of the weak contribution around 4.7 Å, due to the M-M SS signal of the octahedron diagonal (R_{M2}). For the three cases, differently to the hydroxylated cases, the 3D model obtained from the Rietveld refinement of XRPD data in the highly symmetric *Fm-3m* space group was inadequate to simulate the experimental datum. The origin of this failure was, obviously due to the inability of the model to account for two different R_{M1} and R_{M2} distances. For both UiO-66 [101] and UiO-67 [102] cases, the failure of the XRPD model was overcome by using the optimized geometry obtained by ab initio periodic calculations.

The inorganic cornerstones of the as synthesized materials are perfect $M_6(OH)_4O_4$ octahedron (see model in Figure 14b), with 6 equivalent M at the vertex, 12 equivalent M-M1 sides and 3 equivalent and M-M2 diagonals. Upon desolvation 2 structural water molecules are lost per cornerstone unit (Figure 14a), that evolves from $M_6(OH)_4O_4$ to M_6O_6 [101,102,104,105] The new M_6O_6 octahedron compressed (2 opposite vertexes approaching, see model in Figure 14c) resulting in the shortening of 8 of the 12 edges, and the elongation of the other 4 edges. To take into account this variation we simulated the EXAFS contribution

with two independently parameterized paths fixing for the degeneration a ratio of 1/3 and 2/3 with respect to the case of the single contribution. For the three systems, this combined XRPF, EXADS and DFT approach allowed a full interpretation of the EXAFS data in both hydroxylated and dehydroxylated forms [101,102,104,105]. Please note that IR spectroscopy was determinant to confirm this model as allowed to observe the disappearance of the O-H stretching band in these materials.

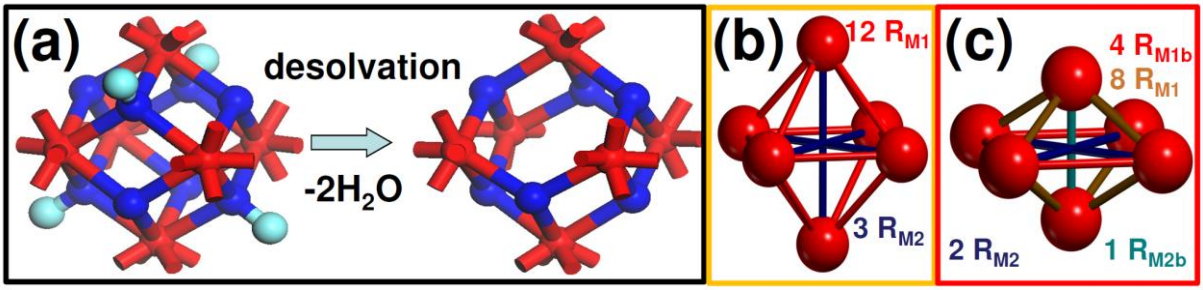

Figure 14. Part (a): Stick and ball representation of the dehydroxylation undergone by the inorganic $M_6O_4(OH)_4$ cornerstone upon thermal treatment at 300 °C in vacuo resulting in a distorted M_6O_6 cluster (M =Zr or Hf). Red, blue and cyan colors refer to M, O and H atoms, respectively. Part (b): Stick and ball representation of the perfect M_6 octahedron, showing 12 equivalent R_{M1} sides and 3 equivalent R_{M2} = $\sqrt{2}$ R_{M1} diagonals. Part (c): Stick and ball representation of a squeezed M_6 octahedron. The 12 sides are now split into 4 in-plane long M_{M1b} sides and 8 prismatic short M_{M1a} sides, while the 3 diagonals evolve into 2 in-plane long M_{M2b} and 1 orthogonal short M_{M2a} diagonals. For clarity, O atoms are omitted in parts (b) and (c). Unpublished Figure.

Table 4. Summary of the EXAFS refinement obtained on the hydroxylated and dehydroxylated forms of UiO-66, UiO-67 and Hf-UiO-66. Parameters without error bars were not optimized. The EXAFS refinement of the hydroxylated materials was obtained using as input model the optimized structure from Rietveld refinement of the corresponding XRPD patterns. The EXAFS refinement of the dehydroxylated materials was obtained using as input model optimized *ab initio* calculations for the hydroxylated of UiO-66. With this approach the coordination number (N) of each contribution is fixed by the model stoichiometry. Refinement of the experimental amplitude is done by optimizing the overall amplitude factor S_0^2 only. The fitting of the higher shells was possible only adopting the axial compressed model of the M_6O_6 octahedron represented where eight octahedron sides R_{M1} are split into eight short prismatic distances (R_{M1}, N=8/3) and four long planar ones (R_{M1b}, N=4/3) and where the three diagonals R_{M2} are split into a short axial diagonal and (R_{M2a}, involving two M atoms out of six; N=1/3) and two long planar diagonals (R_{M2b}, involving four M atoms out of six; N=2/3): Figure 14c. Unpublished table, reporting data from Refs. [100] [101,102,104,105].

	UiO-66	Hydro UiO-67	Hf-UiO-66	UiO-66	UiO-67	Hf-UiO-66
		hydroxylated			dehydroxylated	
T (K)	300	300	300	300	300	573
R-factor	0.01	0.04	0.02	0.02	0.04	0.05
Δk (Å^{-1})	2.0-18.0	2.0-16.2	2.0-16.0	2.0-15.0	2.0-15.0	2.0-15.0
ΔR (Å)	1.0-5.3	1.0-5.3	1.0-5.5	1.0-5.3	1.0-5.3	1.0-3.9
Indip. points	43	38	40	35	35	25
N. variables	14	13	10	15	15	9
ΔE_0 (eV)	5 ± 1	1 ± 1	2.2 ± 0.6	5	1	2.4 ± 0.7
S_0^2	1.17 ± 0.08	1.17	0.91 ± 0.06	1.17	1.17	0.91
$R_{\mu3\text{-}O}$ (Å)	2.087 ± 0.008	2.12 ± 0.02	2.12 ± 0.01	2.06 ± 0.01	2.096 ± 0.007	2.06 ± 0.01
$\sigma^2(\mu_3\text{-}O)$ (Å^2)	0.0036±0.0009	0.005 ± 0.002	0.005 ±0.002	0.008 ± 0.003	0.006 ± 0.001	0.009 ± 0.002
R_{O1} (Å)	2.235 ± 0.008	2.26 ± 0.01	2.25 ± 0.01	2.221 ± 0.007	2.249 ± 0.007	2.19 ± 0.01
σ^2(O1) (Å^2)	0.0074±0.0008	0.006 ± 0.001	0.005	0.007 ± 0.002	0.004 ± 0.001	0.009
R_C (Å)	3.19 ± 0.02	3.40 ± 0.06	3.23 ± 0.06	3.17 ± 0.04	3.15 ± 0.04)	3.22 ± 0.05
σ^2(C) (Å^2)	0.004 ± 0.002	0.012 ± 0.002	0.014 ± 0.011	0.009 ± 0.009	0.004 ± 0.003	0.016 ± 0.013
R_{M1} (Å)	3.511 ± 0.007	3.512 ± 0.006	3.510 ± 0.005	3.35 ± 0.01	3.365 ± 0.015	3.31 ± 0.03
σ^2(M1) (Å^2)	0.007 ± 0.001	0.004 ± 0.001	0.0042 ± 0.0004	0.009 ± 0.001	0.009 ± 0.002	0.009 ± 0.004
R_{M1b} (Å)	-	-	-	3.74 ± 0.02	3.80 ± 0.03	3.45 ± 0.06
σ^2(M1b) (Å^2)	-	-	-	0.009 ± 0.002	0.008 ± 0.003	0.009
R_{M2} (Å)	4.99 ± 0.04	4.95 ± 0.03	4.964	4.14 ± 0.07)	4.15 ± 0.07	-
σ^2(M2) (Å^2)	0.010 ± 0.006	0.004 ± 0.002	0.008 ± 0.002	0.008 ± 0.006	0.006 ± 0.004	-
R_{M2b} (Å)	-	-	-	5.30 ± 0.04	5.46 ± 0.05	-
σ^2(M2b) (Å^2)	-	-	-	0.008	0.006	-

Summarizing, EXAFS spectroscopy allowed to detect the evolution from $M_6(OH)_4O_4$ to M_6O_6 (M = Zr or Hf) of the inorganic cornerstones of UiO-66, UiO-67 and Hf-UiO-66 MOFs occurring in the desolvation process, that escaped XRPD detection. On Zr-UiO-66 and Zr-UiO-67, period calculations performed with CRYSTAL code [109] at DFT level of theory support EXAFS data.

7. Applications of X-ray micro beam: electroabsorption modulated laser for optoelectronic devices

Synchrotron radiation X-ray micro- and nano-beams are emerging characterization tools with broad implications for science, ranging from solid state physics to structural biology. In the last years space-resolved characterization at the (sub-)micrometric scale was made possible by the exponential increase in X-ray brilliance at III generation synchrotron radiation sources and by the impressive improvements in X-ray focusing devices [110]. In the field of materials characterization, they are becoming a key tool for the space-resolved determination of structural (XRD) [111-114] and electronic (XANES/EXAFS) properties [115,116] and for chemical speciation (XRF) [117-120] of nano-structured or composite materials.

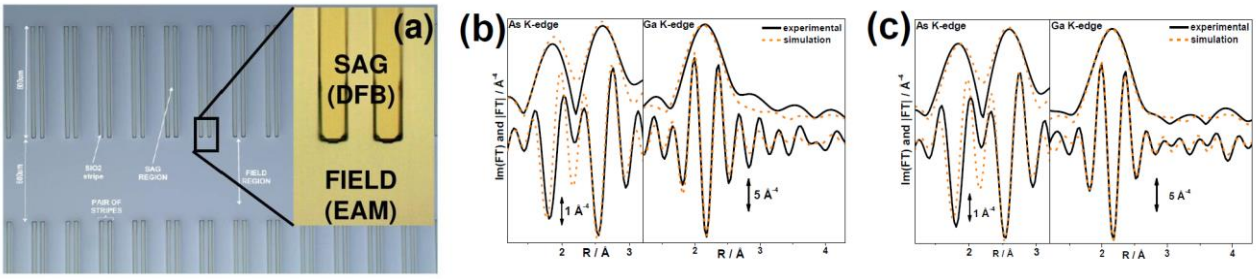

Figure 15. Part **(**a): Optical micrograph of the InP substrate patterned with SiO_2 stripes which allow SAG growth. Part (b): k^3-weighed, phase uncorrected, Fourier Transform modulus and imaginary part of Ga and As K-edges, performed in the SAG region. For the fit a co-refinement approach was adopted. Part (c): As part (b) for the FIELD region. Unpublished Figure reporting data published in Ref. [116].

In particular synchrotron radiation micro-/nano-beams can also be successfully employed to study devices based on nanostructured inorganic materials. An interesting example is represented by the electroabsorption modulated laser (EML) [121,122]. Indeed, nowadays heterostructures based on quaternary III-V semiconductor alloys are widely used in optical communication systems. Advanced optoelectronic devices often require the integration of two different functions in the same chip: excellent results in the development of monolithic integration have been reached with the Selective Area Growth (SAG) technique [123,124]. SAG exploits the perturbation of the growth fluxes induced by a dielectric mask: when the metallorganic precursors collide with the dielectric mask, they are deflected and they can migrate through the unmasked semiconductor where the growth can start. In this way the reactive species coming from the gas phase are enriched by those deflected by the mask: the result is a variation in composition and thickness of semiconductors grown near (SAG region) and far (FIELD region) from the mask (see Figure 15a). The EML, obtained by monolithic integration of an electroabsorption modulator (EAM) with a distributed feedback laser (DFB), is one of the most promising applications of SAG. A voltage modulation applied to the EAM switches it between an opaque and a transparent state by means of the Stark effect and ensures the modulation of the DFB laser emission, allowing long-distance communications (up to 80 km) at high frequency (10 Gb/s).

Mino *et al.* [116] investigated a SAG EML device based on $Al_{xw}Ga_{yw}In_{1-xw-yw}As$ / $Al_{xb}Ga_{yb}In_{1-xb-yb}As$ (compressive-strained well / tensile-strained barrier) MQW structures grown on InP by metallorganic vapor phase epitaxy. They reported reported μ-EXAFS spectra acquired at the ESRF ID22 beamline employing a pair of Kirkpatrick–Baez (KB) mirrors to reach a beam size of 1.7 μm (vertical) × 5.3 μm (horizontal), which allowed them to study in a space resolved way the atomic local environment in the SAG and FIELD regions.

Table 5. Summary of the parameters optimized in the fitting of the EXAFS data (Figure xxb-c) on the SAG and FIELD regions (see Figure 15). A co-refinement approach on As and Ga K-edges was adopted Unpublished Table reporting data published in Ref. [116].

	SAG	**FIELD**
R_{As-Ga} (Å)	2.469 ± 0.007	2.463 ± 0.005
ΔR_{As-Ga} (Å)	0.021 ± 0.007	0.015 ± 0.005
R_{As-In} (Å)	2.60 ± 0.02	2.60 ± 0.02
ΔR_{As-In} (Å)	-0.02 ± 0.02	-0.02 ± 0.02
R_{As-Al} (Å)	2.49 ± 0.11	2.48 ± 0.11
σ^2_{As-Ga} (Å^2)	0.006 ± 0.002	0.005 ± 0.002
σ^2_{As-In} (Å^2)	0.008 ± 0.003	0.007 ± 0.003
σ^2_{As-Al} (Å^2)	0.010 ± 0.004	0.008 ± 0.004

By performing a combined fit of Ga and As K-edges spectra (see Figure 15b-c and Table 5), they observed a stretching of the As-Ga first shell bond distances and a contraction of the As-In first shell distances with respect to the binary compounds InAs and GaAs. These distances are in agreement with experimental [125] and theoretical [126] data on strained $In_{0.60}Ga_{0.40}As$ alloys on InP. Moreover they noticed that ΔR_{As-Ga} is higher in the SAG then in the FIELD region and an higher structural disorder (monitored by the σ^2 values) is observed in the SAG region, however the quality of the data resulted in too high error bars that did not allow them to reliably discriminate between SAG and FIELD regions (see Table 5).

References and Notes.

[1] Margaritondo G. Introduction to Synchrotron Radiation. New York, Oxford, 1988.
[2] Wille K. Synchrotron radiation sources. Rep. Prog. Phys. 1991; 54: 1005-1068.
[3] Bilderback DH, Elleaume P, Weckert E. Review of third and next generation synchrotron light sources. J. Phys. B-At. Mol. Opt. Phys. 2005; 38: S773-S797.
[4] Couprie ME, Filhol JM. X radiation sources based on accelerators. C. R. Phys. 2008; 9: 487-506.
[5] Sandstrom DR, Lytle FW. Developments in Extended X-ray Absorption Fine Structure applied to chemical systems. Ann. Rev. Phys. Chem. 1979; 30: 215-238.
[6] Lee PA, Citrin PH, Eisenberger P, Kincaid M. Extended x-ray absorption fine structure-its strengths and limitations as structural tool. Rev. Mod. Phys. 1981; 53: 769-806.
[7] Teo BK, Joy DC. EXAFS Spectroscopy: Techniques and Applications New York, Plenum, 1981.
[8] Stern EA. Theory of EXAFS. In: Koningsberger DC, Prins R, ed. X-Ray Absorption: Principles, Applications, Techniques of EXAFS, SEXAFS and XANES. New York: John Wiley & Sons, 1988: 3-51.
[9] Filipponi A, Di Cicco A, Natoli CR. X-ray-absorption spectroscopy and n-body distribution functions in condensed matter .1. Theory. Phys. Rev. B 1995; 52: 15122-15134.
[10] Filipponi A, Di Cicco A. X-ray-absorption spectroscopy and n-body distribution functions in condensed matter .2. Data analysis and applications. Phys. Rev. B 1995; 52: 15135-15149.
[11] Rehr JJ, Albers RC. Theoretical approaches to x-ray absorption fine structure. Rev. Mod. Phys. 2000; 72: 621-654.
[12] Boscherini F. X-ray absorption fine structure in the study of semiconductor heterostructures and nanostructures. In: Lamberti C, ed. Characterization of Semiconductor Heterostructures and Nanostructures. Amsterdam: Elsevier, 2008: 289-330.
[13] Bordiga S, Groppo E, Agostini G, van Bokhoven JA, Lamberti C. Reactivity of surface species in heterogeneous catalysts probed by in situ x-ray absorption techniques. Chem. Rev. 2013; 113: dx.doi.org/10.1021/cr2000898.
[14] Bart JCJ, Vlaic G. Extended x-ray absorption fine-structure studies in catalysis. Adv. Catal. 1987; 35: 1-138.
[15] Sinfelt JH, Meitzner GD. X-ray absorption-edge studies of the electronic-structure of metal-catalysts. Accounts Chem. Res. 1993; 26: 1-6.
[16] Newton MA, Dent AJ, Evans J. Bringing time resolution to EXAFS: recent developments and application to chemical systems. Chem. Soc. Rev. 2002; 31: 83-95.
[17] Bare SR, Ressler T. Characterization of catalysts in reactive atmospheres by X-ray absorption spectroscopy. Adv. Catal. 2009; 52: 339-465.
[18] Alexeev O, Gates BC. EXAFS characterization of supported metal-complex and metal-cluster catalysts made from organometallic precursors. Top. Catal. 2000; 10: 273-293.
[19] Sinfelt JH. Structure of bimetallic clusters. Accounts Chem. Res. 1987; 20: 134-139.
[20] Frenkel A. Applications of Extended X-ray Absorption Fine-Structure spectroscopy to studies of bimetallic nanoparticle catalysts. Chem. Soc. Rev. 2012; 41: 7965-7965

[21] Abruna HD. Probing Electrochemical Interfaces with X-Rays. Adv. Chem. Phys. 1990; 77: 255-335.
[22] Abruna HD, Bommarito GM, Yee HS. X-Ray Standing Waves and Surface EXAFS Studies of Electrochemical Interfaces. Accounts Chem. Res. 1995; 28: 273-279.
[23] Bordiga S, Bonino F, Lillerud KP, Lamberti C. X-ray absorption spectroscopies: useful tools to understand metallorganic frameworks structure and reactivity. Chem. Soc. Rev. 2010; 39: 4885-4927.
[24] Riggsgelasco PJ, Stemmler TL, Pennerhahn JE. XAFS of dinuclear metal sites in proteins and model compounds. Coord. Chem. Rev. 1995; 144: 245-286.
[25] Pellerito L, Nagy L. Organotin(IV)$^{n+}$ complexes formed with biologically active ligands: equilibrium and structural studies, and some biological aspects. Coord. Chem. Rev. 2002; 224: 111-150.
[26] Penner-Hahn JE. Characterization of "spectroscopically quiet" metals in biology. Coord. Chem. Rev. 2005; 249: 161-177.
[27] Strange RW, Ellis M, Hasnain SS. Atomic resolution crystallography and XAFS. Coord. Chem. Rev. 2005; 249: 197-208.
[28] Denecke MA. Actinide speciation using X-ray absorption fine structure spectroscopy. Coord. Chem. Rev. 2006; 250: 730-754.
[29] Chen JG. NEXAFS investigations of transition metal oxides, nitrides, carbides, sulfides and other interstitial compounds. 1997; 30: 5-152.
[30] Lamberti C. The use of synchrotron radiation techniques in the characterization of strained semiconductor heterostructures and thin films. Surf. Sci. Rep. 2004; 53: 1-197.
[31] Le Toquin R, Paulus W, Cousson A, Prestipino C, Lamberti C. Time-resolved in situ studies of oxygen intercalation into $SrCoO_{2.5}$, performed by neutron diffraction and X-ray absorption spectroscopy. J. Am. Chem. Soc. 2006; 128: 13161-13174.
[32] Fermi E. Eine statistische Methode zur Bestimmung einiger Eigenschaften des Atoms und ihre Anwendung auf die Theorie des periodischen Systems der Elemente. Z. Phys. 1928; 48: 73-79.
[33] Fermi E. Nuclear Physics. Chicago, University of Chicago Press, 1950.
[34] Borfecchia E, Garino C, Salassa L, Lamberti C. Synchrotron ultrafast techniques for photoactive transition metal complexes. Phil. Trans. R. Soc. A 2013: in press.
[35] Sayers DE, Stern EA, Lytle FW. New technique for investigating noncrystalline structures: fourier analysis of the extended X-ray Absorption Fine Structure. Phys. Rev. Lett. 1971; 27: 1204-1207.
[36] Lytle FW, Sayers DE, Stern EA. Extended x-ray-absorption fine-structure technique. II. Experimental practice and selected results. Phys. Rev. B 1975; 11: 4825-4835.
[37] Estephane J, Groppo E, Damin A, Vitillo JG, Gianolio D, Lamberti C, Bordiga S, Prestipino C, Nikitenko S, Quadrelli EA, Taoufik M, Basset JM, Zecchina A. Structure and enhanced reactivity of chromocene carbonyl confined inside cavities of NaY zeolite. J. Phys. Chem. C 2009; 113: 7305-7315.
[38] Silversmit G, Vekemans B, Nikitenko S, Bras W, Czhech V, Zaray G, Szaloki I, Vincze L. Polycapillary-optics-based micro-XANES and micro-EXAFS at a third-generation bending-magnet beamline. J. Synchrot. Radiat. 2009; 16: 237-246.
[39] Westre TE, Kennepohl P, DeWitt JG, Hedman B, Hodgson KO, Solomon EI. A multiplet analysis of Fe K-edge 1s → 3d pre-edge features of iron complexes. J. Am. Chem. Soc. 1997; 119: 6297-6314.
[40] Koningsberger DC, Prins R. X-ray Absorption: Principles, Applications, Techniques of EXAFS, SEXAFS, and XANES. New York, US, John Wiley & Sons, 1988.
[41] Harris DC, Bertolucci MD. Symmetry and spectroscopy an introduction to vibrational and electronic spectroscopy. New York, US, Dover Publications, 1989.
[42] Lamberti C, Prestipino C, Bonino F, Capello L, Bordiga S, Spoto G, Zecchina A, Moreno SD, Cremaschi B, Garilli M, Marsella A, Carmello D, Vidotto S, Leofanti G. The chemistry of the oxychlorination catalyst: an in situ, time-resolved XANES study. Angew. Chem. Int. Edit. 2002; 41: 2341-2344.
[43] Muddada NB, Olsbye U, Caccialupi L, Cavani F, Leofanti G, Gianolio D, Bordiga S, Lamberti C. Influence of additives in defining the active phase of the ethylene oxychlorination catalyst. Physical Chemistry Chemical Physics 2010; 12: 5605-5618.
[44] Muddada NB, Olsbye U, Leofanti G, Gianolio D, Bonino F, Bordiga S, Fuglerud T, Vidotto S, Marsella A, Lamberti C. Quantification of copper phases, their reducibility and dispersion in doped-$CuCl_2/Al_2O_3$ catalysts for ethylene oxychlorination. Dalton Trans. 2010; 39: 8437-8449.
[45] Piovano A, Agostini G, Frenkel AI, Bertier T, Prestipino C, Ceretti M, Paulus W, Lamberti C. Time resolved in situ XAFS study of the electrochemical oxygen intercalation in $SrFeO_{2.5}$ Brownmillerite structure: Comparison with the homologous $SrCoO_{2.5}$ system. Journal of Physical Chemistry C 2011; 115: 1311-1322.
[46] Lamberti C, Palomino GT, Bordiga S, Berlier G, D'Acapito F, Zecchina A. Structure of homoleptic $Cu^{I}(CO)_3$ cations in Cu^{I}exchanged ZSM-5 zeolite: An X-ray absorption study. Angewandte Chemie-International Edition 2000; 39: 2138-2141.
[47] Ricchiardi G, Damin A, Bordiga S, Lamberti C, Spanò G, Rivetti F, Zecchina A. Vibrational structure of Titanium silicate catalysts. A spectroscopic and theoretical study. 2001; 123: 11409-11419.
[48] Belli M, Scafati A, Bianconi A, Mobilio S, Palladino L, Reale A, Burattini E. X-ray absorption near edge structures (XANES) in simple and complex Mn compounds. Solid State Commun. 1980; 35: 355-361.

[49] Bianconi A, Bauer RS. Evidence of SiO at the Si-oxide interface by surface soft X-ray absorption near edge spectroscopy. Surf. Sci. 1980; 99: 76-86.
[50] Oudenhuijzen MK, van Bokhoven JA, Miller JT, Ramaker DE, Koningsberger DC. Three-site model for hydrogen adsorption on supported platinum particles: Influence of support ionicity and particle size on the hydrogen coverage. J. Am. Chem. Soc. 2005; 127: 1530-1540.
[51] Bianconi A, Doniach S, Lublin D. X-ray Ca K edge of calcium adenosine triphosphate system and of simple Ca compunds. Chem. Phys. Lett. 1978; 59: 121-124.
[52] Bressler C, Chergui M. Ultrafast X-ray absorption spectroscopy. Chem. Rev. 2004; 104: 1781-1812.
[53] Stern EA. Theory of the extended x-ray-absorption fine structure. Phys. Rev. B 1974; 10: 3027-3037.
[54] Teo B-K, Lee PA. Ab initio calculations of amplitude and phase functions for extended x-ray absorption fine structure spectroscopy. J. Am. Chem. Soc. 1979; 101: 2815-2832.
[55] McKale AG, Veal BW, Paulikas AP, Chan SK, Knapp GS. Improved ab initio calculations of amplitude and phase functions for extended x-ray absorption fine structure spectroscopy. J. Am. Chem. Soc. 1988; 110: 3763-3768.
[56] For a compilation of electron inelastic mean free path lengths (λ) in solids for energies in the range 0–10 000 eV above the Fermi level, see e.g. Seah MP, Dench WA. Quantitative electron spectroscopy of surfaces: A standard data base for electron inelastic mean free paths in solids. Surf. Interface Anal., 1979; 1: 2-11.
[57] Filipponi A. EXAFS for liquids. J. Phys.-Condes. Matter 2001; 13: R23-R60.
[58] Debye P. Interferenz von Röntgenstrahlen und Wärmebewegung. Ann. Phys. 1913; 348: 49-92.
[59] Waller I. Zur Frage der Einwirkung der Wärmebewegung auf die Interferenz von Röntgenstrahlen. Z. Phys. 1923; 17: 398-408.
[60] Asakura K. Analysis of EXAFS. In: Iwasawa Y, ed. X-ray absorption fine structure for catalysts and surfaces. Singapore: World Scientific, 1996: 33-58.
[61] Nyquist H. Certain topics in telegraph transmission theory. Trans. AIEE 1928; 47: 617–644. Reprinted in Proc. IEEE **2002 20***90* **2**280-**2**305.
[62] Shannon CE. Communication in the presence of noise. Proc. Institute Radio Engin. 1949; 37: 10–21. Reprinted in *Proc. IEEE* 1988 19**86** 1447.
[63] Newmann MN. Encyclopedia of Polymer Science and Engineering. New York, Wiley, 1985.
[64] Leofanti G, Marsella A, Cremaschi B, Garilli M, Zecchina A, Spoto G, Bordiga S, Fisicaro P, Berlier G, Prestipino C, Casali G, Lamberti C. Alumina-supported copper chloride 3. Effect of exposure to ethylene. J. Catal. 2001; 202: 279-295.
[65] Leofanti G, Marsella A, Cremaschi B, Garilli M, Zecchina A, Spoto G, Bordiga S, Fisicaro P, Prestipino C, Villain F, Lamberti C. Alumina-supported copper chloride - 4. Effect of exposure to O-2 and HCl. J. Catal. 2002; 205: 375-381.
[66] Leofanti G, Padovan M, Garilli M, Carmello D, Marra GL, Zecchina A, Spoto G, Bordiga S, Lamberti C. Alumina-supported copper chloride 2. Effect of aging and thermal treatments. J. Catal. 2000; 189: 105-116.
[67] Leofanti G, Padovan M, Garilli M, Carmello D, Zecchina A, Spoto G, Bordiga S, Palomino GT, Lamberti C. Alumina-supported copper chloride 1. Characterization of freshly prepared catalyst. J. Catal. 2000; 189: 91-104.
[68] Prestipino C, Bordiga S, Lamberti C, Vidotto S, Garilli M, Cremaschi B, Marsella A, Leofanti G, Fisicaro P, Spoto G, Zecchina A. Structural determination of copper species on the alumina-supported copper chloride catalyst: A detailed EXAFS study. J. Phys. Chem. B 2003; 107: 5022-5030.
[69] Joyner RW, Martin KJ, Meehan P. Some applications of statistical tests in analysis of EXAFS and SEXAFS Data. J. Phys. C: Solid State Phys. 1987; 20: 4005-4012.
[70] Lee PA, Beni G. New method for the calculation of atomic phase shifts: Application to extended x-ray absorption fine structure (EXAFS) in molecules and crystals. Phys. Rev. B 1977; 15: 2862-2883.
[71] Muddada NB, Olsbye U, Fuglerud T, Vidotto S, Marsella A, Bordiga S, Gianolio D, Leofanti G, Lamberti C. The role of chlorine and additives on the density and strength of Lewis and Bronsted acidic sites of γ-Al_2O_3 support used in oxychlorination catalysis: A FTIR study. J. Catal. 2012; 284: 236-246.
[72] Gianolio D, Muddada NB, Olsbye U, Lamberti C. Doped-$CuCl_2/Al_2O_3$ catalysts for ethylene oxychlorination: Influence of additives on the nature of active phase and reducibility. Nucl. Instrum. Met. Phys. Res. B 2012; 284: 53-57.
[73] Lamberti C, Bordiga S, Bonino F, Prestipino C, Berlier G, Capello L, D'Acapito F, Xamena FXLI, Zecchina A. Determination of the oxidation and coordination state of copper on different Cu-based catalysts by XANES spectroscopy in situ or in operando conditions. Phys. Chem. Chem. Phys. 2003; 5: 4502-4509.
[74] Coperet C, Chabanas M, Saint-Arroman RP, Basset JM. Homogeneous and heterogeneous catalysis: Bridging the gap through surface organometallic chemistry. Angew. Chem.-Int. Edit. 2003; 42: 156-181.
[75] Davis ME. Ordered porous materials for emerging applications. Nature 2002; 417: 813-821.
[76] Ozin GA, Gil C. Intrazeolite organometallics and coordination-complexes - internal versus external confinement of metal guests. 1989; 89: 1749-1764.
[77] Karol FJ, Brown GL, Davison JM. Chromocene-based catalysts for ethylene polymerization: Kinetic parameters. J. Polym. Sci. A 1973; 11: 413 - 424.
[78] Thomas JL, Brintzinger HH. Molybdenocene as an intermediate in reactions with hydroogen, nitrogen, and carbon monoxide. J. Am. Chem. Soc. 1972; 94: 1386-1387.

[79] Tang Wong KL, Brintzinger HH. Reactivity patterns of chromocene, molybdenocene, and tungstenocene reaction systems. I. Carbonyl complex formation as a probe of coordinative unsaturation. J. Am. Chem. Soc. 1975; 97: 5143-5146.
[80] Brintzinger HH, Lohr LL, Tang Wong KL. Reactivity patterns of chromocene, molybdenocene, and tungstenocene reaction systems. II. Analysis in terms of molecular orbital and electron-electron repulsion energies. J. Am. Chem. Soc. 1975; 97: 5146-5155.
[81] Estephane J, Groppo E, Vitillo JG, Damin A, Lamberti C, Bordiga S, Zecchina A. Chromocene in porous polystyrene: an example of organometallic chemistry in confined spaces. Phys. Chem. Chem. Phys. 2009; 11: 2218-2227.
[82] Gianolio D, Groppo E, Estephane J, Prestipino C, Nikitenko S, Zecchina A, Bordiga S, Taoufik M, Quadrelli EA, Basset JM, Lamberti C. Formation and reactivity of Cr(II) carbonyls hosted in polar and non polar supports. J. Phys.: Conf. Series 2009; 190.
[83] Estephane J, Groppo E, Vitillo JG, Damin A, Gianolio D, Lamberti C, Bordiga S, Quadrelli EA, Basset JM, Kervern G, Emsley L, Pintacuda G, Zecchina A. A multitechnique approach to spin-flips for $Cp_2Cr(II)$ chemistry in confined state. J. Phys. Chem. C 2010; 114: 4451-4458.
[84] Marra GL, Fitch AN, Zecchina A, Ricchiardi G, Salvalaggio M, Bordiga S, Lamberti C. Cation location in dehydrated Na-Rb-Y zeolite: An XRD and IR study. J. Phys. Chem. B 1997; 101: 10653-10660.
[85] Gordon KR, Warren KD. Spectroscopic and magnetic studies of the 3d metallocenes. Inorg. Chem. 1978; 17: 987-994.
[86] Ozin GA, Godbert J. Intrazeolite metallocenes: chemistry, spectroscopy, and dynamics. 1989; 93: 878-893.
[87] Note that the scheme is not strictly rigorous. The electronic transitions should be expressed in terms of group theory, once that all the possible excited configurations have been taken into account. The arrows representing bands **I**, **II** and **III** have to be considered only as simplified way to illustrate which electron is undergoing a transition and towards which type of molecular orbital. Notwithstanding the lack of a rigorous language, Figure 7b has the advantage to show in an easy way and with a single scheme the origin of both the optical absorptions and the XANES features of $CrCp_2$ molecules. This scheme represents one of the few attempts in literature to match the information obtained with these two techniques. .
[88] Warren KD. Ligand field theory of metal sandwich complexes. Configurations. Inorg. Chem. 1974; 13: 1243-1246.
[89] Muraoka PT, Byun D, Zink JI. Wavelength dependence of photooxidation vs photofragmentation of chromocene. J. Phys. Chem. A 2001; 105: 8665-8671.
[90] Brennan J, Cooper G, Green JC, Payne MP, Redfern CM. A study of valence level photoelectron cross-sections for the metallocenes of vanadium, chromium, cobalt and nickel from 20 to 100 eV. J. Electron Spectrosc. Relat. Phenom. 1993; 66: 101-115.
[91] Chetwynd-Talbot J, Grebenik P, Perutz RN. Photochemical reactions of M $(\eta-C_5H_5)_2L_n$ (M = W, Mo, Cr, V) in low-temperature matrices. Detection of tungstenocene and molybdenocene. Inorg. Chem. 1982; 21: 3641-3651.
[92] Lavrentyev AA, Nikiforov IY, Dubeiko VA, Gabrelian BV, Rehr JJ. The use of the FEFF8 code to calculate the XANES and electron density of states of some sulfides. J. Synchrot. Radiat. 2001; 8: 288-290.
[93] Ankudinov AL, Rehr JJ. Development of XAFS theory. J. Synchrot. Radiat. 2003; 10: 366-368.
[94] Ruiz-Lopez MF, Loos M, Goulon J, Benfatto M, Natoli CR. Reinvestigation of the EXAFS and XANES spectra of ferrocene and nickelocene in the framework of the multiple scattering theory. Chem. Phys. 1988; 121: 419-437.
[95] Lamberti C, Bordiga S, Geobaldo F, Zecchina A, Otero Arean C. Stretching frequencies of cation CO adducts in alkali-metal exchanged zeolites - an elementary electrostatic approach. J. Chem. Phys. 1995; 103: 3158-3165.
[96] Salassa L, Ruiu T, Garino C, Pizarro AM, Bardelli F, Gianolio D, Westendorf A, Bednarski PJ, Lamberti C, Gobetto R, Sadler PJ. EXAFS, DFT, light-Induced nucleobase binding, and cytotoxicity of the photoactive complex cis-$[Ru(bpy)_2(CO)Cl]^+$. Organometallics 2010; 29: 6703-6710.
[97] Bonino F, Chavan S, Vitillo JG, Groppo E, Agostini G, Lamberti C, Dietzel PDC, Prestipino C, Bordiga S. Local structure of CPO-27-Ni metallorganic framework upon dehydration and coordination of NO. Chem. Mat. 2008; 20: 4957-4968.
[98] Salassa L, Garino C, Salassa G, Nervi C, Gobetto R, Lamberti C, Gianolio D, Bizzarri R, Sadler PJ. Ligand-selective photodissociation from $[Ru(bpy)(4AP)_4]^{2+}$: a spectroscopic and computational study. Inorg. Chem. 2009; 48: 1469-1481.
[99] Salassa L, Gianolio D, Garino C, Salassa G, Borfecchia E, Ruiu T, Nervi C, Gobetto R, Bizzarri R, Sadler PJ, Lamberti C. Structure of $[Ru(bpy)_n(AP)_{(6-2n)}]^{2+}$ homogeneous complexes: DFT calculation vs. EXAFS. J. Phys.: Conf. Ser. 2009; 190: 012141.
[100] Cavka JH, Jakobsen S, Olsbye U, Guillou N, Lamberti C, Bordiga S, Lillerud KP. A new zirconium inorganic building brick forming metal organic frameworks with exceptional stability. J. Am. Chem. Soc. 2008; 130: 13850-13851.
[101] Valenzano L, Civalleri B, Chavan S, Bordiga S, Nilsen MH, Jakobsen S, Lillerud KP, Lamberti C. Disclosing the complex structure of UiO-66 Metal Organic Framework: A synergic combination of experiment and theory. Chem. Mat. 2011; 23: 1700-1718.

[102] Chavan S, Vitillo JG, Gianolio D, Zavorotynska O, Civalleri B, Jakobsen S, Nilsen MH, Valenzano L, Lamberti C, Lillerud KP, Bordiga S. H_2 storage in isostructural UiO-67 and UiO-66 MOFs. Phys. Chem. Chem. Phys. 2012; 14: 1614-1626.
[103] Kandiah M, Nilsen MH, Usseglio S, Jakobsen S, Olsbye U, Tilset M, Larabi C, Quadrelli EA, Bonino F, Lillerud KP. Synthesis and stability of tagged UiO-66 Zr-MOFs. Chem. Mater. 2010; 22: 6632-6640.
[104] Jakobsen J, Gianolio D, Wragg D, Nilsen MH, Emerich H, Bordiga S, Lamberti C, Olsbye U, Tilset M, Lillerud KP. Structural determination of a highly stable metal-organic framework with potentials in interim radioactive waste scavenging: Hf-UiO-66. Phys. Rev. B 2012; 86: art. n. 125429.
[105] Gianolio D, Vitillo JG, Civalleri B, Bordiga S, Olsbye U, Lillerud KP, Valenzano L, Lamberti C. Combined study of structural properties on metal-organic frameworks with same topology but different linkers or metal. J. Phys.: Conf. Ser. 2013: in press.
[106] Milanesio M, Artioli G, Gualtieri AF, Palin L, Lamberti C. Template burning inside TS-1 and Fe-MFI molecular sieves: An in situ XRPD study. J. Am. Chem. Soc. 2003; 125: 14549-14558.
[107] Hafizovic J, Bjorgen M, Olsbye U, Dietzel PDC, Bordiga S, Prestipino C, Lamberti C, Lillerud KP. The inconsistency in adsorption properties and powder XRD data of MOF-5 is rationalized by framework interpenetration and the presence of organic and inorganic species in the nanocavities. J. Am. Chem. Soc. 2007; 129: 3612-3620.
[108] Agostini G, Lamberti C, Palin L, Milanesio M, Danilina N, Xu B, Janousch M, van Bokhoven JA. In situ XAS and XRPD parametric Rietveld refinement to understand dealumination of Y zeolite catalyst. J. Am. Chem. Soc. 2010; 132: 667-678.
[109] Dovesi R, Orlando R, Civalleri B, Roetti C, Saunders VR, Zicovich-Wilson CM. CRYSTAL: a computational tool for the ab initio study of the electronic properties of crystals. Z. Kristallogr. 2005; 220: 571-573.
[110] Martinez-Criado G, Borfecchia E, Mino L, Lamberti C. Micro and nano X-ray beams. In: Agostini G, Lamberti C, ed. Characterization of Semiconductor Heterostructures and Nanostructures II. Amsterdam: Elsevier, 2013.
[111] Kazimirov A, Bilderback DH, Huang R, Sirenko A, Ougazzaden A. Microbeam high-resolution diffraction and X-Ray Standing Wave methods applied to semiconductor structures. J. Phys. D-Appl. Phys. 2004; 37: L9-L12.
[112] Kazimirov A, Sirenko AA, Bilderback DH, Cai ZH, Lai B, Huang R, Ougazzaden A. Synchrotron high angular resolution microdiffraction analysis of selective area grown optoelectronic waveguide arrays. J. Phys. D-Appl. Phys. 2006; 39: 1422-1426.
[113] Mino L, Gianolio D, Agostini G, Piovano A, Truccato M, Agostino A, Cagliero S, Martinez-Criado G, Codato S, Lamberti C. Structural characterization of Multi-Quantum Wells in electroabsorption-modulated lasers by using synchrotron radiation micrometer-beams. Adv. Mater. 2010; 22: 2050-2054.
[114] Cagliero S, Borfecchia E, Mino L, Calore L, Bertolotti F, Martinez-Criado G, Operti L, Agostino A, Truccato M, Badica P, Lamberti C. Insight into non-linearly shaped superconducting whiskers via a synchrotron nanoprobe. Superconduct. Sci. Technol. 2012; 25: 125002.
[115] Truccato M, Lamberti C, Prestipino C, Agostino A. Evidence of ion diffusion at room temperature in microcrystals of the $Bi_2Sr_2CaCu_2O_{8+\delta}$ superconductor. Appl. Phys. Lett. 2005; 86: Art. n. 213116.
[116] Mino L, Gianolio D, Agostini G, Piovano A, Truccato M, Agostino A, Cagliero S, Martinez-Criado G, d'Acapito F, Codato S, Lamberti C. μu-EXAFS, μu-XRF, and μu-PL characterization of a Multi-Quantum-Well electroabsorption modulated laser realized via selective area growth. Small 2011; 7: 930-938.
[117] Sirenko AA, Reynolds CL, Peticolas LJ, Ougazzaden A, Kazimirov A, Huang R, Fontes E, Bilderback D. Micro-X-ray fluorescence and micro-photoluminescence in InGaAsP and InGaAs layers obtained by selective area growth. J. Cryst. Growth 2003; 253: 38-45.
[118] Mino L, Agostino A, Codato S, Lamberti C. Study of epitaxial selective area growth $In_{1-x}Ga_xAs$ films by synchrotron μ-XRF mapping. J. Anal. At. Spectrom. 2010; 25: 831-836.
[119] Mino L, Agostino A, Codato S, Martinez-Criado G, Lamberti C. Effect of selective area growth mask width on multi-quantum-well electroabsorption modulated lasers investigated by synchrotron radiation X-ray microprobe. Nucl. Instr. Meth. Phys. Res. B 2012; 284: 6-9.
[120] Borfecchia E, Mino L, Gianolio D, Groppo C, Malaspina N, Martinez-Criado G, Sans JA, Poli S, Castelli D, Lamberti C. Iron oxidation state in garnet from a subduction setting: a micro-XANES and electron microprobe ("flank method") comparative study. J. Anal. At. Spectrom. 2012; 27: 1725-1733.
[121] Salvatore RA, Sahara RT, Bock MA, Libenzon I. Electroabsorption modulated laser for long transmission spans. IEEE J. Quantum Electron. 2002; 38: 464-476.
[122] Foti E, Fratta L, Ghiglieno F, Coriasso C, Cacciatore C, Rigo C, Agresti M, Vallone M, Codato S, Fornuto G, Fang R, Rosso M, Buccieri A, Valenti P. Optimisation of 10 Gbit/s InGaAsP electroabsorption modulator operating at high temperature. IEE Proc.-Optoelectron. 2004; 151: 103-108.
[123] Gibbon M, Stagg JP, Cureton CG, Thrush EJ, Jones CJ, Mallard RE, Pritchard RE, Collis N, Chew A. Selective-area low-pressure MOCVD of GaInAsP and related materials on planar InP substrates. Semicond. Sci. Technol. 1993; 8: 998-1010.
[124] Coltrin ME, Mitchell CC. Mass transport and kinetic limitations in MOCVD selective-area growth. J. Cryst. Growth 2003; 254: 35-45.

[125] Romanato F, De Salvador D, Berti M, Drigo A, Natali M, Tormen M, Rossetto G, Pascarelli S, Boscherini F, Lamberti C, Mobilio S. Bond-lengthvariation in $In_xGa_{1-x}As$/InP strained epitaxial layers. Phys. Rev. B 1998; 57: 14619-14622.
[126] d'Acapito F. Nearest-neighbor distances in strained thin films of random pseudobinary semiconductor alloys: A calculational methodology. J. Appl. Phys. 2004; 96: 369-373.